



In-plume and out-of-plume analysis of aerosol–cloud interactions derived from the 2014–2015 Holuhraun volcanic eruption

Amy H. Peace^{1,3}, Ying Chen², George Jordan³, Daniel G. Partridge¹, Florent Malavelle³, Eliza Duncan¹, and Jim M. Haywood^{1,3}

¹Faculty of Environment, Science and Economy, University of Exeter, Exeter, EX4 4QE, UK

²School of Geography, Earth and Environmental Sciences, University of Birmingham, Birmingham, B15 2TT, UK

³Met Office, Exeter, EX1 3PB, UK

Correspondence: Amy H. Peace (amy.peace@metoffice.gov.uk)

Received: 6 February 2024 – Discussion started: 8 February 2024

Revised: 3 June 2024 – Accepted: 27 June 2024 – Published: 29 August 2024

Abstract. Aerosol effective radiative forcing (ERF) has persisted as the most uncertain aspect of anthropogenic forcing over the industrial period, limiting our ability to constrain estimates of climate sensitivity and to confidently predict 21st century climate change. Aerosol–cloud interactions are the most uncertain component of aerosol ERF. The 2014–2015 Holuhraun volcanic eruption acted as a large source of sulfur dioxide, providing an opportunistic experiment for studying aerosol–cloud interactions at a climatically relevant scale. We evaluate the observed aerosol-induced perturbation to marine liquid cloud properties inside the volcanic plume in the first month of the eruption and compare the results to those from UKESM1 (UK Earth System Model). In the first 2 weeks, as expected, we find an in-plume shift to smaller and more numerous cloud droplets in both the observations and the simulations. We find an observed increase in liquid water path (LWP) values inside the plume that is not captured in UKESM1. However, in the third week, the in-plume shift to smaller and more numerous cloud droplets is neither observed nor modelled, and there are discrepancies between the observed and modelled response in the fourth week. An analysis of the model simulations and trajectory modelling reveals that air mass history and background meteorological factors can strongly influence aerosol–cloud interactions between the weeks of our analysis. Overall, our study supports the findings of many previous studies: the aerosol impact on cloud effective radius is significant, with differences in the observed and modelled response for in-cloud LWP.

1 Introduction

The evolution of aerosol emissions is thought to have profoundly impacted climate over the industrial period. The increasing emission of anthropogenic aerosols and their gaseous precursors has exerted a negative radiative forcing on the climate system through the interaction of aerosols with clouds and radiation (Bellouin et al., 2020). The negative radiative forcing of aerosols has masked a proportion of warming from rising greenhouse gas emissions (Eyring et al., 2021) and led to large-scale changes in the water cycle and atmospheric circulation (Douville et al., 2021). Over the

coming decades reductions in anthropogenic aerosol emissions are expected due to more ambitious climate change and air quality mitigation policies (Rao et al., 2017). Despite the importance of aerosol–climate interactions, aerosol radiative forcing is the most uncertain component of anthropogenic radiative forcing over the industrial period (Forster et al., 2021). The uncertainty in the magnitude of aerosol radiative forcing impacts the accuracy with which we can project near-term future climate changes (Andreae et al., 2005; Seinfeld et al., 2016; Peace et al., 2020; Watson-Parris and Smith, 2022). Aerosol–cloud interactions (ACIs) make up the largest component of the uncertainty in aerosol radiative forcing (Bel-

louin et al., 2020). It is therefore an important task to continue to improve our understanding of ACIs to predict future climate change more confidently.

Marine low-level liquid clouds strongly reflect shortwave radiation. Only small changes in their properties can have a significant impact of the radiative balance of the Earth system (Wood, 2012). Understanding how aerosols modify the properties of these clouds has therefore been the focus of much research. Conceptually, aerosols modify the properties of clouds through a chain of events (e.g. Haywood and Boucher, 2000). Firstly, aerosols act as cloud condensation nuclei (CCN). An increase in aerosol leads to an increase in cloud droplet number concentrations (N_d) and, for a constant amount of cloud water, a reduction in cloud droplet effective radius (r_{eff}). Smaller and more numerous cloud droplets increase the albedo of clouds (Twomey, 1974). These effects have been widely observed (e.g. Bréon et al., 2002; Feingold et al., 2003). An increase in N_d may initiate further adjustments to cloud properties, such as changes in liquid water path (LWP) and cloud fraction, although bidirectional responses in LWP to an increase in N_d have been observed (e.g. Toll et al., 2019) and simulated (e.g. Ackerman et al., 2004). The directionality of the LWP response likely depends on the meteorological conditions present and accordingly whether smaller cloud droplets lead to precipitation suppression, which can potentially increase LWP (Albrecht, 1989; Pincus and Baker, 1994), or if the smaller droplets lead to enhanced evaporation and decreased sedimentation, which can enhance entrainment and decrease LWP (Ackerman et al., 2004; Bretherton et al., 2007). Recent research has shown significant cancellation of the positive and negative LWP responses is likely at large scales resulting in a weak LWP response to increased aerosol globally (Toll et al., 2019). However, global climate models (GCMs) can disagree with evidence from observations and higher-resolution models on the magnitude and sign of the LWP response to increased N_d (Toll et al., 2017; Gryspeerd et al., 2019). The uncertain response of LWP to increased N_d demonstrates why cloud adjustments to an increase in N_d remain poorly constrained despite being able to enhance or counteract an increase in cloud albedo due to an increase in smaller cloud droplets.

“Opportunistic” experiments offer a way to improve our understanding of aerosol–cloud interactions in a system where both the aerosol-perturbed and unperturbed background cloud states are reasonably well established (Christensen et al., 2022). The magnitude and sign of ACIs can depend on numerous factors including background aerosol concentrations, meteorology and cloud properties (e.g. Stevens and Feingold, 2009; Carslaw et al., 2013). Opportunistic experiments can therefore provide a way to isolate ACIs in environments with similar conditions or provide insight into how background conditions affect ACIs. Key opportunistic experiments that have been used to study ACIs include ship tracks, industrial plumes, wildfires and volcanic eruptions (e.g. Malavelle et al., 2017; Toll et al., 2017; Christensen et

al., 2022). In this study, we utilise the 2014–2015 Holuhraun effusive volcanic eruption as an opportunistic experiment to assess and improve our understanding of ACIs.

The 2014–2015 Holuhraun eruption in Iceland (64.85° N, 16.83° W) began on 31 August 2014 and ended on 27 February 2015. This eruption was one of the largest sources of tropospheric volcanic emissions since the 1783–1784 Laki eruption (Ilyinskaya et al., 2017). Ground-based and satellite observations show that the Holuhraun eruption emitted large amounts of SO_2 (up to $\sim 100 \text{ kt SO}_2 \text{ d}^{-1}$) into the troposphere (Pfeffer et al., 2018; Carboni et al., 2019). The daily SO_2 emitted from the eruption was at least a factor of 3 larger than anthropogenic emissions from the whole of Europe (Schmidt et al., 2015). Once emitted, SO_2 is readily oxidised into sulfate aerosol; therefore, the Holuhraun eruption created a large aerosol plume. As a result, the 2014–2015 Holuhraun eruption provides an opportunistic experiment to investigate ACI hypotheses at a large, climatically relevant scale.

A handful of studies have leveraged the Holuhraun eruption to study ACIs using differing approaches. Malavelle et al. (2017) used a climatological approach to identify aerosol–cloud interactions following the eruption. Their results showed a decrease in r_{eff} during October 2014 in both satellite observations and climate model simulations compared to the climatological mean. Yet, satellite observations revealed no clear perturbation to LWP or cloud fraction, unlike climate model responses showing varying LWP changes. Chen et al. (2022) used a machine learning approach to predict the cloud properties that would be expected for September and October 2014 without the presence of the volcanic eruption given the meteorological conditions. The predicted cloud properties were then compared to satellite observations to isolate the aerosol perturbation to cloud properties following the eruption. Similarly to the climatological approach of Malavelle et al. (2017), the machine learning approach isolated a decrease in r_{eff} but no detectable change in LWP. However, the machine learning approach revealed an aerosol-induced increase in cloud fraction. Lastly, Haghghatnasab et al. (2022) focused on the first week following the eruption, comparing cloud properties inside and outside the SO_2 eruption plume in satellite observations and a high-resolution model. This plume analysis approach showed an increase in N_d and decrease in r_{eff} inside the eruption plume in line with the results from Malavelle et al. (2017) and Chen et al. (2022). However, Haghghatnasab et al. (2022) show an observed shift in the distribution of in-plume LWP values, with a decreased likelihood of low LWP values and an increased likelihood of higher LWP values, which is further exaggerated in the high-resolution model.

Our study builds on these previous analyses of aerosol–cloud interactions derived for September 2014. We use satellite observations of aerosol and cloud properties to evaluate the observed ACIs following the start of the volcanic eruption and compare our results to simulations from UKESM1

(UK Earth System Model). We add to the plume analysis approach utilised in Haghghatnasab et al. (2022) by using a more detailed plume masking method that isolates areas close to the plume that are likely to be more representative of the cloud fields being perturbed. We also extend the plume analysis from the first week of September 2014 that was analysed in Haghghatnasab et al. (2022) to the rest of the month. The eruption was at its most powerful in September 2014 with large amounts of SO₂ released that then reduced during October 2014 (Carboni et al., 2019). The 4-week time period allows us to investigate how air mass history and background meteorological factors influence aerosol–cloud interactions between the weeks of our analysis using the HYSPLIT trajectory model (Hybrid Single-Particle Lagrangian Integrated Trajectory model). A week-by-week analysis is performed showing that the aerosol conditions in the first 2 weeks and the last week of September are close to pristine, but during the third week, the background aerosol is significantly perturbed owing to air mass trajectories originating over continental Europe. This breakdown into weeks provides a convenient framework for developing statistical analyses over the month.

2 Data and methods

2.1 Defining a plume mask from satellite observations of SO₂

We use the column amount of SO₂ in the lower troposphere to define a plume mask that is used to compare cloud properties inside and outside of the aerosol plume following the eruption.

We obtain the SO₂ data product from the Ozone Mapping and Profiler Suite (OMPS) Nadir Mapper (NM) on board the NASA–NOAA Suomi National Polar-orbiting partnership (SNPP) satellite that was launched in October 2011 (Flynn et al., 2014; Seftor et al., 2014). The Nadir Mapper is a UV spectrometer that measures backscattered solar UV radiance from the Earth and solar irradiance. SO₂ absorbs strongly in the UV, and therefore the vertical column density of SO₂ can be retrieved from satellite measurements of the UV spectrum. The column amount of SO₂ is retrieved from OMPS using a principal component analysis (PCA) algorithm (Li et al., 2017, 2020b). We use V2.0 of the SO₂ data product in our analysis (NMSO2_PCA_L2 V2.0) (Li et al., 2020a).

The PCA algorithm provides six estimates of the total SO₂ vertical column density based on a priori profiles of the centre of mass altitude (Li et al., 2020a). We use the data product that is based on an SO₂ plume height in the lower troposphere (TRL) at 3 km, which is a typical height of volcanic degassing and moderate eruptions. Carboni et al. (2019) showed the altitude of the centre of mass of the SO₂ Holuhraun eruption plume was mainly confined to within 0–6 km. Following the OMPS quality control procedure, pixels

near the edge of the swath and where the solar zenith angle (SZA) > 70° are excluded. OMPS has a nadir resolution of 50 km × 50 km and crosses the Equator at about 13:30 LT. We resample swath data into a regular grid with resolution of 1.0° × 1.0° using a nearest-neighbour method. The 1.0° × 1.0° resolution is the same as the dataset of cloud property observations that we use. When creating the plume mask for use with the model simulations, we first re-grid the 1.0° × 1.0° OMPS data to the coarser resolution of the model simulations. The OMPS SO₂ vertical column density is unavailable 1 d in each week, and we exclude these dates from our analysis. We apply the following analysis in a “Holuhran” domain of longitude 45° W to 30° E and latitude 45 to 80° N (e.g. as in Fig. 1).

After processing the SO₂ data product to gridded data, the next step in our analysis is to define a suitable plume mask and bounding region around the plume to use in isolating in-plume vs. out-of-plume cloud properties. We use a threshold exceedance approach to define the eruption plume mask. We define grid cells where the total column amount of SO₂ > 1 DU (Dobson units) as being in-plume. This masking approach and threshold exceedance choice was also used in Haghghatnasab et al. (2022). Next, for each day we define a bounding box around the plume as the minimum to maximum latitude and longitude of the plume extent. We use this bounding box approach rather than using the whole domain to minimise differences in meteorological conditions between inside and outside the plume, which can confound the aerosol effect on cloud properties (e.g. D. T. McCoy et al., 2020). The plume mask and bounding region for each day is shown in Animation S1 in the Supplement.

2.2 Satellite observations of SO₂ plume height

Nadir spectrometer instruments in the ultraviolet and infrared can be used to deduce information on SO₂ plume altitude (Carboni et al., 2016). The Infrared Atmospheric Sounding Interferometer (IASI) is a Fourier transform interferometer on board the MetOp-A and MetOp-B satellites. SO₂ height information can be obtained from IASI through the optimal estimation retrieval scheme as explained in Carboni et al. (2012, 2016). In the algorithm, retrievals are performed when detection of SO₂ is above a given threshold. The threshold defined for the Holuhraun eruption is 0.49 effective DU (Carboni et al., 2019). The retrieval algorithm determines SO₂ column amount and the altitude (mean of a Gaussian profile) of the SO₂ plume. We use the output from the IASI retrieval to compare the height of the volcanic SO₂ plume against cloud top height.

2.3 Satellite observations of cloud properties

We use products of the MODerate resolution Imaging Spectroradiometer (MODIS) on board the polar-orbiting Aqua and Terra satellites (Platnick et al., 2015) to evaluate per-

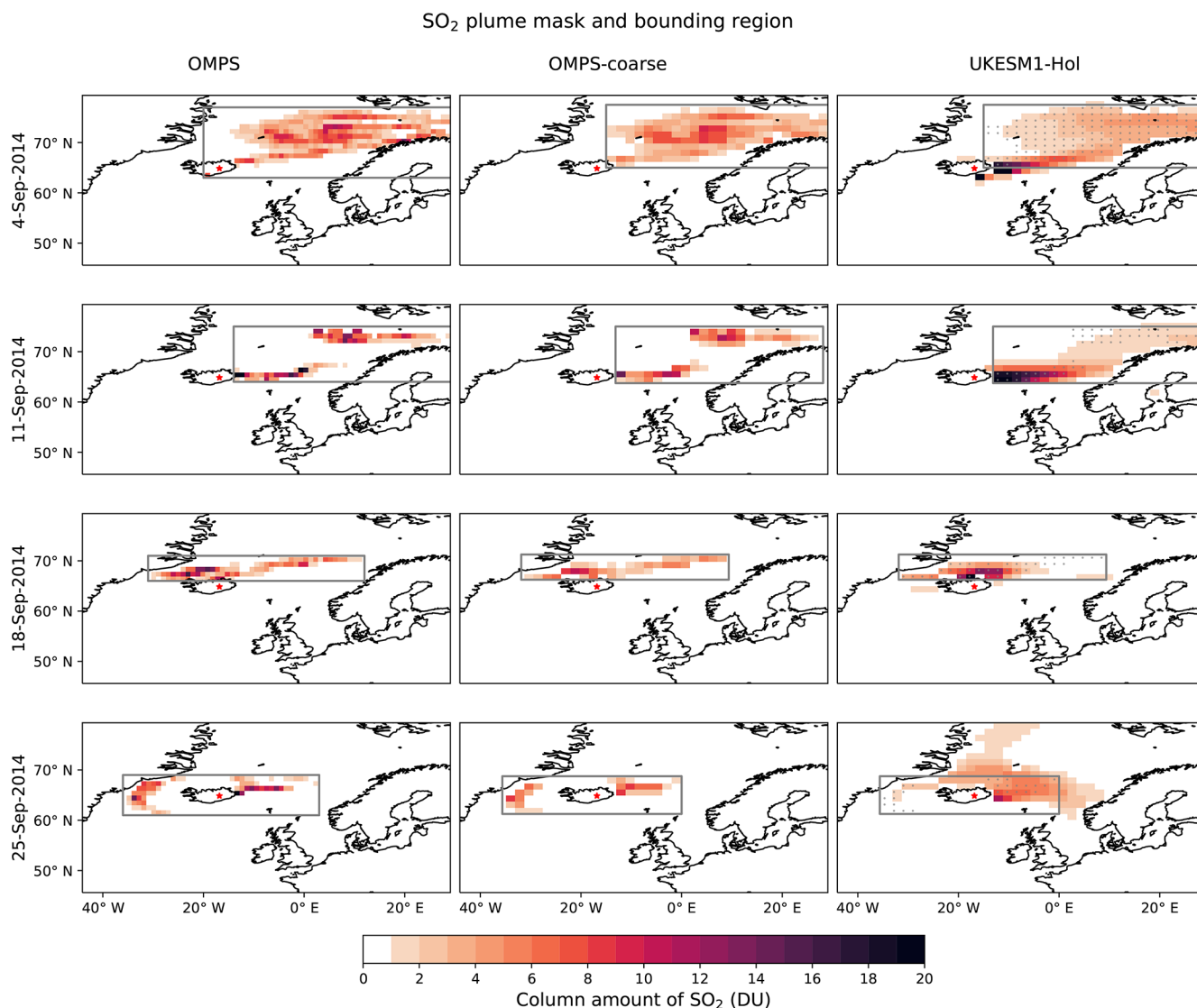


Figure 1. Total column amount of SO₂ (Dobson units) retrieved from OMPS ($1.0^{\circ} \times 1.0^{\circ}$) and OMPS-coarse (OMPS re-gridded to UKESM1-Hol resolution) and simulated in UKESM1-Hol within the plume mask for the midweek day of the 4 weeks in September 2014 being analysed. The plume mask is defined where the total amount of SO₂ exceeds 1 DU. The grey box shows the bounding box region surrounding the plume mask within which we conduct our in-plume vs. out-of-plume analysis. The grey dots in the UKESM1-Hol column show the location of the OMPS-coarse plume mask used in the model comparison. The red star shows the location of the eruption site.

turbations to cloud properties inside the SO₂ plume as determined in Sect. 2.1. We use the MODIS COSP (Cloud Feedback Model Intercomparison Project (CFMIP) Observation Simulator Package) Level 3 daily (MCD06COSP) dataset that combines pixel-scale observations from Terra (MODO6_L2) and Aqua (MYDO6L2) into a regular $1^{\circ} \times 1^{\circ}$ grid (Pincus et al., 2023). We use the mean of the sampled Level 2 pixels in each Level 3 grid. The dataset was recently produced to facilitate comparison with results from the COSP MODIS simulator, which is a software tool that can be employed in climate models to produce data comparable to satellite observations. The definitions of variables

within this dataset are more in line with the MODIS simulator than standard MODIS products. Therefore, the MODIS COSP dataset is particularly useful for observation–model comparison. We analyse marine liquid N_d , r_{eff} , in-cloud LWP and cloud fraction. In the Level 2 MODIS products, r_{eff} , cloud water path and cloud optical thickness are retrieved from observed multispectral reflectances using a radiative transfer model at 1 km nadir resolution. Cloud phase is retrieved through the phase retrieval algorithm at 1 km resolution (Platnick et al., 2017).

We derive liquid N_d from liquid cloud r_{eff} and cloud optical thickness (τ_c) assuming an adiabatic cloud:

$$N_d = \alpha \tau_c^{0.5} r_{\text{eff}}^{-2.5}, \quad (1)$$

where α is $1.375 \times 10^{-5} \text{ m}^{-0.5}$. Only data pixels where cloud optical thickness is between 4 and 70 and r_{eff} between 4 and $30 \mu\text{m}$ are retained where the retrieval is the most reliable (Quaas et al., 2006), but N_d derived in this way is still subject to uncertainties related to the cloud adiabaticity assumption and uncertainty in underlying cloud property retrievals (Gryspeerd et al., 2022). We use the liquid cloud retrieval fraction rather than cloud mask fraction to study cloud fraction. The cloud retrieval fraction is lower than the cloud mask fraction in most regions as it excludes pixels identified as sunglint, heavy aerosol or partly cloudy (Pincus et al., 2023).

In addition, we use the Level 2 Collection 6.1 MODIS Aqua products (Platnick et al., 2015, 2017) sampled to a $0.5^\circ \times 0.5^\circ$ grid to obtain cloud top height for comparison with the IASI observations of SO_2 plume altitude.

2.4 UKESM1 simulations

We conduct a model simulation of the Holuhraun eruption and a corresponding control simulation with no volcanic emissions using the atmosphere-only version 1.0 of the UK Earth System Model (hereafter UKESM1-A) (Sellar et al., 2019; Mulcahy et al., 2020). We compare the perturbation of in-plume cloud properties observed from MODIS to these simulations, and we also use the UKESM1-A simulations to further investigate the influence of meteorology on aerosol–cloud interactions.

UKESM1 is the first version of the UK Earth System Model and contributed to the sixth Coupled Model Intercomparison Project (CMIP6) (Eyring et al., 2016; Sellar et al., 2019). UKESM1 is based on the HadGEM3-GC3.1 physical climate model (Kuhlbrodt et al., 2018; Williams et al., 2018) coupled to several Earth system processes including interactive stratosphere–troposphere chemistry from the UK Chemistry and Aerosol model (UKCA) (Archibald et al., 2020). In the atmosphere-only version of UKESM1 (UKESM1-A), sea surface temperatures and sea ice concentrations are prescribed from the Program for Climate Model Diagnosis and Intercomparison (Rayner et al., 2003). Vegetation and ocean biological fields are prescribed from a member of the UKESM1 CMIP6 historical ensemble (Sellar et al., 2019).

The aerosol scheme within UKCA is the modal version of the Global Model of Aerosol Processes (GLOMAP-mode), which simulates new particle formation; gas-to-gas particle transfer; aerosol coagulation; cloud processing of aerosol; and deposition of sulfate, sea salt, black carbon and particulate organic matter (Mann et al., 2010; Mulcahy et al., 2020). Mineral dust is simulated separately using the CLAS-SIC dust scheme (Woodward, 2001). The aerosol chemistry is coupled to the UKCA stratospheric–tropospheric aerosol scheme where chemical oxidants are interactively

simulated (Archibald et al., 2020). UKCA uses aspects of the Unified Model Global Atmosphere (GA7.1; Walters et al., 2019) within the UKESM for the large-scale advection, convective transport and boundary layer mixing of aerosol. Aerosol particles are activated into cloud droplets using the Abdul-Razzak and Ghan (2000) activation scheme. Large-scale cloud microphysics is a single-moment scheme based on Wilson and Ballard (1999) with improvements based on Boutle et al. (2014). Changes in cloud droplet number concentration (N_d) can impact cloud droplet effective radius (Jones et al., 2001) and the autoconversion of cloud liquid water to rainwater through the Khairoutdinov and Kogan (2000) scheme. Aerosol–cloud interactions are simulated in large-scale liquid clouds. Convection is parameterised separately to large-scale clouds and does not consider aerosol. Bulk properties of large-scale clouds are simulated using the prognostic cloud fraction and prognostic condensate (PC2) scheme (Wilson et al., 2008a, b) with the modification described in Morcrette (2012). The GA7.1 model and its coupling to UKCA are described in further detail in Walters et al. (2019) and Mulcahy et al. (2020).

We use global model simulations with a resolution of N96L85, which is a horizontal resolution of $1.875^\circ \times 1.25^\circ$ ($\sim 208 \text{ km} \times 139 \text{ km}$ at the Equator and $\sim 86 \text{ km} \times 139 \text{ km}$ near the Holuhraun eruption site), with 85 atmospheric levels. The model resolution is coarser than the MODIS and OMPS datasets we use that are at $1.0^\circ \times 1.0^\circ$ resolution. In the Holuhraun eruption simulation of this UKESM1 setup, the volcanic SO_2 emissions are distributed equally between 0.8 and 3 km in the grid cell containing the eruption vent following the magnitude and altitude profile of emissions (Malavelle et al., 2017). The prescribed volcanic SO_2 emissions vertical profile is in agreement with satellite observations from IASI and shows the SO_2 plume height during September and October 2014 is mostly between 0.8 and 2.5 km (Jordan et al., 2024). We refer to the simulation that includes volcanic emissions as UKESM1-Hol hereafter. A control simulation was also performed without the Holuhraun eruption emissions which we refer to as UKESM1-Ctrl. The control simulation enables us to assess whether any of the differences in our model simulations are simply due to differences in the meteorology rather than due to the aerosol perturbations. The eruption and control simulations include background aerosol emissions from anthropogenic and natural sources. The modelled horizontal winds between approximately 1.3 to 80 km are nudged towards ERA-Interim reanalysis on a 6-hourly timescale to reduce model internal variability. The model output fields are extracted at high temporal resolution (3- or 6-hourly output) for comparison to observational data. The spatial and chemical evolution of the Holuhraun aerosol pollution in these UKESM1-A simulations has recently been evaluated in a multi-model comparison framework in Jordan et al. (2024).

To aid the comparison of modelled cloud properties with MODIS, we use the COSP MODIS simulator for model out-

put where possible (Bodas-Salcedo et al., 2011; Pincus et al., 2012). N_d was calculated from COSP output using the same calculation and filtering as for the MODIS data. Similarly to the MODIS analysis, we focus on marine liquid clouds. In our plume analysis of the model simulations, we use the OMPS SO₂ plume mask that was created from OMPS data re-gridded to the coarser model resolution.

2.5 Trajectory modelling

The Hybrid Single Particle Lagrangian Trajectory (HYSPLIT4) model (Stein et al., 2015) was used to calculate 10 d back trajectories from the Holuhraun eruption vent. For consistency with UKESM1-A simulations, ERA-Interim 6-hourly reanalyses (Dee et al., 2011), re-gridded to $1.0^\circ \times 1.0^\circ$, were used to drive HYSPLIT. For every hour during September 2014, a 27-member ensemble of 10 d backward trajectories was initiated from the eruption site (64.85°N , 16.83°W) at a starting altitude of 2000 m a.g.l. (above ground level). The 27-member ensemble was created to sample the uncertainty associated with location accuracy. The centre trajectory of the ensemble is initialised at the coordinates above, with the remaining 26 members offset by a fixed grid factor of 1.0° of latitude and longitude in the horizontal and 0.01σ units in the vertical, forming a 3-dimensional space with 27 trajectory initialisation points.

We create transport probability function maps to investigate the dominant movement path of the air masses during September 2014. The transport probability function, $P(A_{i,j})$, represents the probability (%) of a backward trajectory passing through a specific grid cell. $A_{i,j}$ was calculated as

$$A_{i,j} = \frac{n_{i,j}}{N}, \quad (2)$$

where $n_{i,j}$ corresponds to the number of distinct trajectory visits within a grid cell, and N corresponds to the total number of trajectories. The maps allow a qualitative assessment of whether the air masses reaching Holuhraun are from geographic areas that are relatively pristine or influenced by anthropogenic emissions, and they also help characterise the thermodynamic properties of those air masses.

3 Results

3.1 Evolution of the Holuhraun SO₂ plume

Our analysis uses the plume masks derived from the observed column amount of SO₂ to isolate cloud properties inside vs. outside the aerosol plume formed from the 2014–2015 Holuhraun eruption (see Sect. 2.1). Variability in meteorology and cloud state across a domain can make the impact of aerosol perturbations to cloud properties difficult to isolate, for example, if the aerosol-influenced cloud fields experience different conditions than the unperturbed cloud fields

(e.g. Christensen et al., 2022). Therefore, we define a bounding box area around our plume mask to minimise differences in meteorological conditions.

Figure 1 shows a snapshot of the column amount of SO₂ within our plume mask and the corresponding bounding regions for the middle day in each of the 4 weeks in September 2014 that we analyse. Animation S1 in the Supplement shows an animation of the plume mask and bounding region for all the days analysed.

On many of the days in September 2014, the observed SO₂ plume disperses to the north-east of the eruption site. There are a handful of days within the month when the plume was transported towards western Europe where it triggered air pollution events (Ialongo et al., 2015; Schmidt et al., 2015; Boichu et al., 2016; Steensen et al., 2016; Twigg et al., 2016; Zerefos et al., 2017). Our plume masking and bounding box method appears to track the spatial evolution of the observed SO₂ plume well for most days in September.

Figure 1 and Animation S2 show the daily mean total column amount of SO₂ for the UKESM1-Hol simulations and the corresponding plume mask and bounding region when derived from the OMPS-coarse (OMPS re-gridded to UKESM1-Hol resolution) mask. In common with simulations of explosive volcanic eruptions that are nudged to ERA reanalyses (Haywood et al., 2010; Wells et al., 2023), in general the SO₂ plume simulated in the model agrees well with the spatial location of the SO₂ plume observed from OMPS. Jordan et al. (2024) also show that the UKESM1-Hol simulations accurately capture the evolution of the volcanic plume in September and October 2014 when compared to SO₂ retrieved from the IASI (Infrared Atmospheric Sounding Interferometer) satellite instrument. This agreement gives us confidence in using the SO₂ mask derived from observations to evaluate the model simulations, but there may be days when there are differences in the spatial location of the plume and bounding box derived from observations compared to the model simulations (e.g. 25 September). The recommended quality control procedure for OMPS involves excluding pixels where the SZA > 70°. Due to the high latitude of the eruption, this procedure excludes pixels at the top of our domain as September progresses and would also exclude pixels from the MODIS dataset that are less reliable. The column amount of SO₂ in UKESM1-Hol therefore has a further northward extent than the OMPS plume mask towards the end of September.

3.2 Aerosol perturbation to observed in-plume cloud properties

The next stage of our analysis compares cloud properties retrieved from the MODIS COSP dataset inside the SO₂ plume mask to areas outside the plume mask yet still within the bounding region. Figure S2 in the Supplement shows the plume mask bounding region overlaid on MODIS observations of marine liquid cloud N_d and r_{eff} for our snapshot

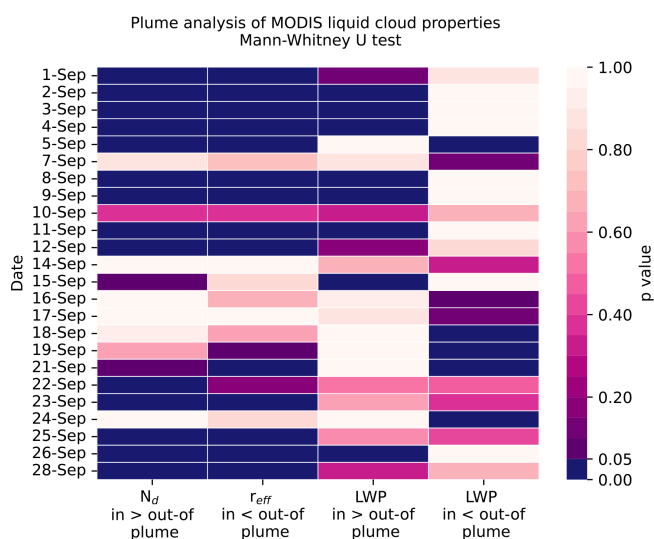


Figure 2. Statistical significance of daily changes in MODIS marine cloud properties inside vs. outside of the SO_2 plume mask. Significance is evaluated using the Mann–Whitney U test. The colour bar displays the p value, with dark blue indicating a statistically significant perturbation to cloud properties inside the plume for that day.

days. This figure gives an indication of the spatial variation in cloud properties across the domain as well as the data coverage.

We evaluate if there is an aerosol-induced perturbation to N_d , r_{eff} , LWP and cloud fraction in marine liquid clouds for days in September 2014. Animations of daily cloud properties and their in-plume vs. out-of-plume distribution are shown in Animations S4–S7. As an example of the daily analysis, Fig. S3 shows the distribution of N_d and r_{eff} in-plume and out-of-plume for our snapshot days. For each day we use the Mann–Whitney U test (Mann and Whitney, 1947) to evaluate if the sample of in-plume cloud properties is significantly different to the sample of the out-of-plume cloud properties. The results of this statistical significance test are summarised in Fig. 2.

In more than half the days we analyse (14 out of 24) observed N_d is statistically significantly higher inside the plume compared to outside. Between 1 to 12 September there are only 2 d (7 and 10 September) when N_d is not higher within the plume. However, between 14 and 21 September no days display significantly higher N_d inside the plume. If we exclude 14 September due to its small sample size (Animation S4), the remaining days in this collection fall within the third week of September, which leads us to aggregate our results into the weeks of September later in the study. In the fourth week of September, 5 of the 6 d analysed have significantly higher N_d within the plume. Across our analysis, all but one of the days that display significantly larger values of N_d in-plume have corresponding statistically significantly smaller values of r_{eff} in-plume. An aerosol-induced

increase in N_d and decrease in r_{eff} is consistent with the Twomey effect (Twomey, 1974), which has been widely observed (e.g. Christensen et al., 2022). Most days (6 out of 9) within the first 2 weeks of September that have an increase in in-plume N_d show a significant increase in LWP. There is 1 d within the first 2 weeks that shows a significant decrease in LWP. Yet the days in the fourth week of September that display an in-plume increase in N_d reveal a different picture with no consistent response in LWP.

To investigate the lack of perturbation to the in-plume N_d for many days of the third week of September and why there is a variation in the in-plume LWP response across September, we aggregate our daily plume analysis into the weeks of September. We also use the weekly aggregated data to compare the observed in-plume perturbation to cloud properties that are simulated by UKESM1-A. Figure 3 shows the weekly in-plume and out-of-plume distributions for N_d and r_{eff} . LWP is shown in Fig. 4. The weekly aggregated results confirm our daily plume analysis; there is a statistically significant increase in N_d and decrease in r_{eff} for the first, second and fourth weeks of September, which is absent in the third week. The sample of in-plume LWP is statistically significantly greater in these 3 weeks but not the third week. We next compare our observed weekly plume analysis results to those from UKESM1-A and use diagnostics available from the model simulations in combination with air mass back-trajectory analysis to untangle the differences in the aerosol perturbation to cloud properties over the first 4 weeks of the Holuhraun eruption.

3.3 Comparison of observed vs. modelled perturbation to in-plume cloud properties

Table 1 shows the area-weighted geometric mean values of marine liquid cloud properties inside and outside of the plume mask and the corresponding in-plume perturbation to cloud properties. The UKESM1-Hol simulation shows significantly greater N_d and significantly smaller r_{eff} inside the plume in the first 2 weeks of September, with no statistically significant perturbation in that direction in the control simulation. The lack of perturbation to N_d and r_{eff} in UKESM1-Ctrl indicates the perturbation to cloud properties inside the plume is not explained by meteorological variability and is therefore aerosol-induced. In the third week, UKESM1-Hol features a significantly decreased N_d inside the plume which is consistent with MODIS and UKESM1-Ctrl. In the fourth week there is a non-significant increase in N_d and decrease in r_{eff} in UKESM1-Hol in comparison to a significant change in the MODIS observations. The statistical significance of daily changes in modelled cloud properties is summarised in Fig. S6.

There is not a significant increase or decrease in in-plume LWP in UKESM1-Hol during the first 2 weeks of September. This contrasts with MODIS where the distribution of in-plume LWP values is significantly greater than out-of-plume

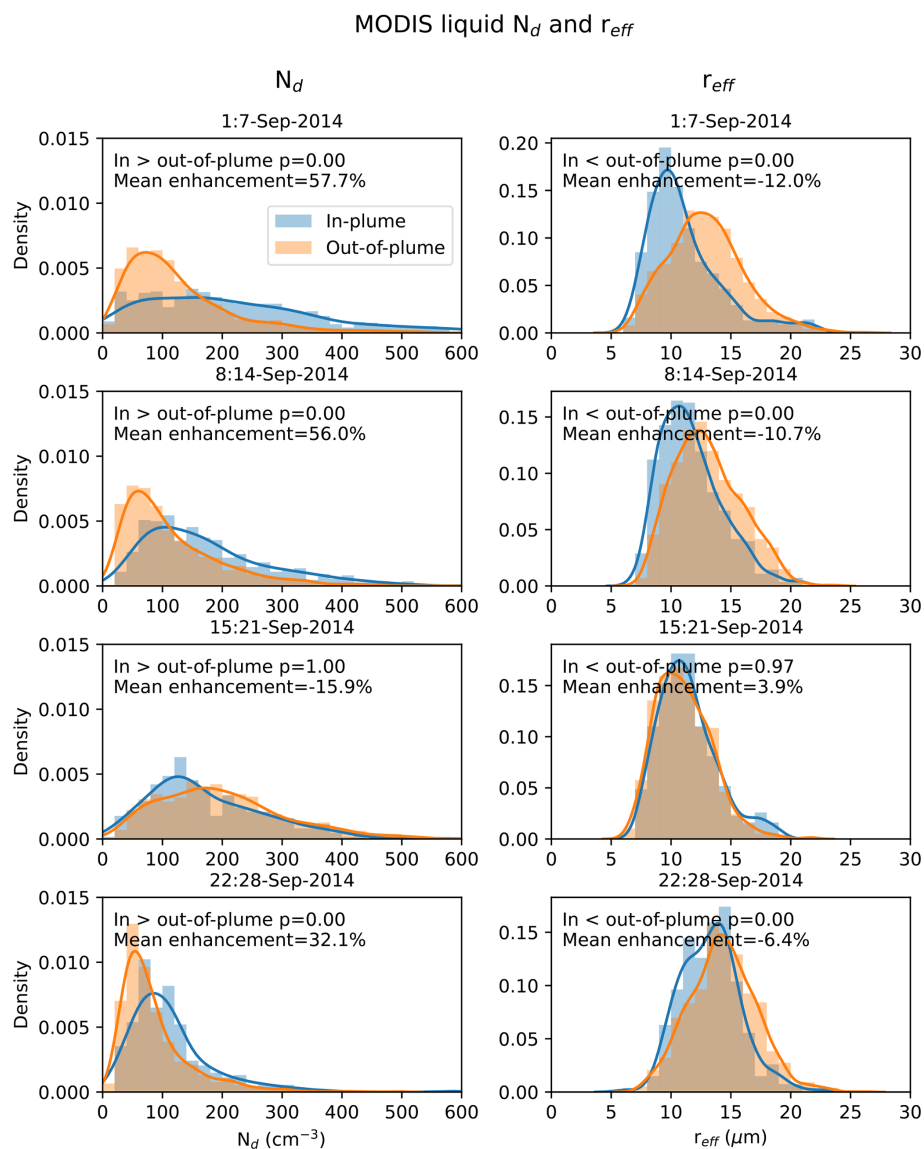


Figure 3. Histogram of MODIS liquid cloud droplet number concentration (cm^{-3}) and effective radius (μm) inside (blue) and outside (orange) the plume mask aggregated by week. Only marine cloud properties are considered. The Mann–Whitney U test is used to calculate if the in-plume N_d is statistically greater than that outside of the plume. The p value and mean in-plume enhancement is displayed for each week.

values. In the third week, there is an observed decrease in LWP inside the plume. The in-plume decrease in LWP is represented in the eruption and control simulations, indicating that the decrease in LWP in the third week could be due to the sampling of different cloud conditions inside the plume rather than an aerosol effect. During the fourth week the distribution of in-plume LWP is statistically greater in MODIS in contrast to an in-plume reduction in LWP in UKESM1-Hol and UKESM1-Ctrl.

We also evaluate perturbations to cloud fraction in our weekly analysis. In the first week the cloud fraction is statistically greater in-plume in MODIS, UKESM1-Hol and UKESM1-Ctrl. The consistency of the increase in in-plume

cloud fraction between UKESM1-Hol and UKESM1-Ctrl indicates that the large in-plume enhancement in cloud fraction is mostly driven from meteorology variability across the field. In the second week, MODIS observations show a more modest statistically significant increase in cloud fraction in-plume, whilst UKESM1-A simulations show a statistically significant decrease in-plume. In the third week in-plume cloud fraction is statistically significantly lower in-plume compared to out-of-plume. Likewise to the first week, the consistency in cloud fraction changes between the UKESM1-Hol and UKESM1-Ctrl indicates this is primarily driven by meteorological variability. In the fourth week there is a non-significant decrease in observed in-plume cloud frac-

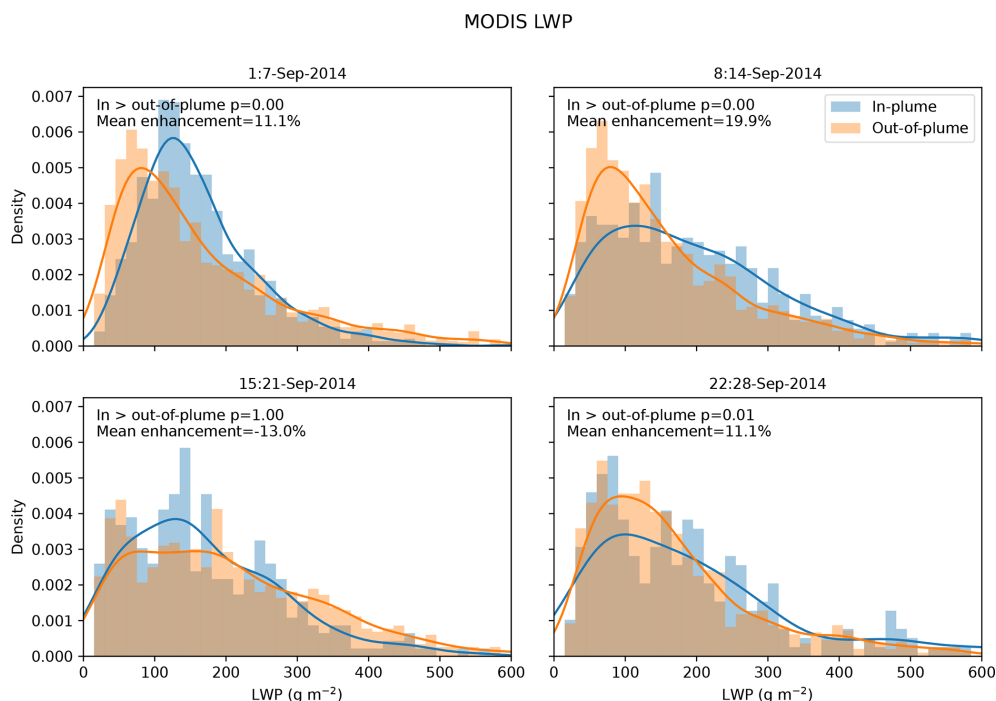


Figure 4. Histogram of MODIS in-cloud liquid water path (g m^{-2}) inside (blue) and outside (orange) the plume mask aggregated by week. Only marine cloud properties are considered. The Mann–Whitney U test is used to calculate if the in-plume LWP is statistically greater than that outside of the plume. The p value and mean in-plume enhancement are displayed for each week.

tion, but the decrease is statistically significant in both model simulations. We tested the robustness of our observed cloud fraction results when using different MODIS cloud fraction variables, as shown in Fig. S5. Total (all phases) cloud retrieval fraction and total cloud mask fraction showed a statistically significant increase in in-plume cloud fraction during the first 2 weeks and decrease in the third week, but the magnitude of response is lower, whereas the direction of the response in the fourth week was of opposite sign to the liquid cloud retrieval fraction.

These results indicate that UKESM1-A captures the observed change in N_d and r_{eff} in the first 2 weeks of September 2014, but there is not a significant change in simulated in-plume LWP during these 2 weeks. The model control simulations help elucidate that changes in cloud properties inside the plume during the third week are likely not due to ACIs. Next, we use the UKESM1-Hol simulation and trajectory modelling to investigate the aerosol–cloud interaction mechanisms at play during the different weeks in September 2014.

3.4 Disentangling aerosol–cloud interaction mechanisms during September 2014

3.4.1 Air mass history

In the previous section we showed that the lack of in-plume perturbation to N_d and r_{eff} in the third week of September

featured in both the MODIS observations and the UKESM1-A Holuhraun simulation. In the third week, the MODIS out-of-plume N_d distribution shown in Fig. 3 more closely resembles the polluted in-plume distributions of N_d than the clean out-of-plume backgrounds. We use back-trajectory modelling to explore the air mass origins during the different weeks of our analysis. Figure 5 shows that during weeks 1, 2 and 4 back trajectories initialised at the eruption site mostly pass through pristine air to the west of Iceland en-route to the Holuhraun eruption site. However, in week 3, a larger proportion of the back trajectories pass over western Europe. The air masses passing over Europe will experience greater aerosol pollution from anthropogenic sources, which is a plausible reason for higher background N_d during week 3. This polluted background is also well simulated by UKESM1-A (Fig. S7).

The activation of the Holuhraun aerosol plume into cloud droplet depends on multiple factors. These factors include the number, size and hygroscopicity of aerosol particles, as well as the updraught velocity at cloud base and the water vapour supersaturation. Reutter et al. (2009) showed the activation of aerosol into cloud droplets can occur under three regimes: updraught-limited, aerosol-limited, or aerosol- and updraught-sensitive regimes. The updraught-limited activation regime is characterised by low ratios of updraught velocity and aerosol number concentration and hence is more likely to occur under polluted air masses, such as week 3 in

Table 1. Weekly area-weighted geometric mean of MODIS and UKESM1-A marine liquid cloud properties inside and outside of the plume mask. The last four columns display the mean in-plume perturbation (%) of each cloud property. The in-plume perturbation is calculated as (mean inside plume – mean outside of plume)/mean outside of plume, where the mean is the area-weighted geometric mean. Bold text in the in-plume perturbations represents where the weekly aggregated in-plume values are statistically greater or less than outside of the plume. Table S1 in the Supplement shows the sample size of N_d weekly aggregated data.

Week		Inside (outside) plume values				In-plume perturbation (%)			
		1	2	3	4	1	2	3	4
N_d (cm ⁻³)	MODIS	148 (94)	147 (94)	144 (172)	95 (72)	58	56	-16	32
	UKESM1-Hol	221 (141)	235 (203)	188 (188)	202 (200)	56	16	-20	8
	UKESM1-Ctrl	85 (105)	93 (103)	101 (130)	105 (123)	-20	-2	-24	-13
r_{eff} (μm)	MODIS	11.1 (12.7)	11.3 (12.7)	11.9 (12.2)	13.0 (13.9)	-12	-11	4	-6
	UKESM1-Hol	9.6 (11.1)	9.4 (9.9)	10.6 (10.0)	10.2 (10.5)	-14	-5	6	-3
	UKESM1-Ctrl	12.5 (12.0)	12.3 (12.3)	12.0 (11.1)	12.3 (12.0)	4	0	8	3
LWP (g m ⁻²)	MODIS	137 (123)	149 (124)	134 (154)	145 (130)	11	20	-13	11
	UKESM1-Hol	110 (107)	110 (116)	75 (109)	125 (135)	3	-5	-31	-8
	UKESM1-Ctrl	93 (100)	85 (92)	79 (103)	113 (132)	-7	-9	-30	-15
Cloud retrieval fraction (%)	MODIS	66 (36)	56 (46)	72 (58)	28 (33)	87	18	-14	-15
	UKESM1-Hol	60 (32)	38 (49)	24 (44)	31 (39)	85	-21	-45	-20
	UKESM1-Ctrl	55 (32)	36 (49)	22 (40)	32 (37)	73	-26	-44	-12

our analysis (Jones et al., 1994; Reutter et al., 2009; Carslaw et al., 2013; Spracklen and Rap, 2013). In this updraught-limited regime the activation of aerosol to cloud droplets depends on updraught velocity rather than aerosol concentration. As a result, under this regime, polluted air masses arriving in the region of the Holuhraun aerosol plume during the third week would be less susceptible to further aerosol-induced increases in N_d . In comparison, in the aerosol-limited region the activation of aerosol to cloud droplets is proportional to the aerosol number concentration.

3.4.2 Background meteorology

We also explore if the meteorological conditions during the weeks of our analysis affect ACIs. During week 3, the in-plume LWP and cloud fraction from the MODIS and UKESM1-A simulations are lower than outside the plume. In the absence of a clear aerosol–cloud interaction inside the Holuhraun plume, a difference in LWP and cloud fraction may indicate the area inside the plume has different meteorological

conditions and cloud properties from those outside of the plume. Figure 6 shows visible satellite imagery in the third week overlaid by the plume mask and bounding box region. On 16–19 September there is a region of clear sky that persists in the north of the bounding box. Since there is agreement between the lack of ACI signal in observations and simulations in the third week, we use the UKESM1-Hol simulation to investigate differences in meteorological conditions during the third week that may contribute towards the negligible in-plume aerosol perturbation to cloud properties.

Figure 7 shows meteorological variables inside the bounding box in the UKESM1-Hol simulation. The model simulations are nudged to ERA-Interim reanalysis horizontal winds and potential temperatures. The third week is noticeably drier in terms of precipitation and relative humidity at 950 hPa, which is representative of the clear-sky region in the north of the bounding box during 16–19 September. There is a slightly lower median and smaller interquartile range of lower-tropospheric stability (LTS) during the third week, but there are many outliers that represent grid cells with higher

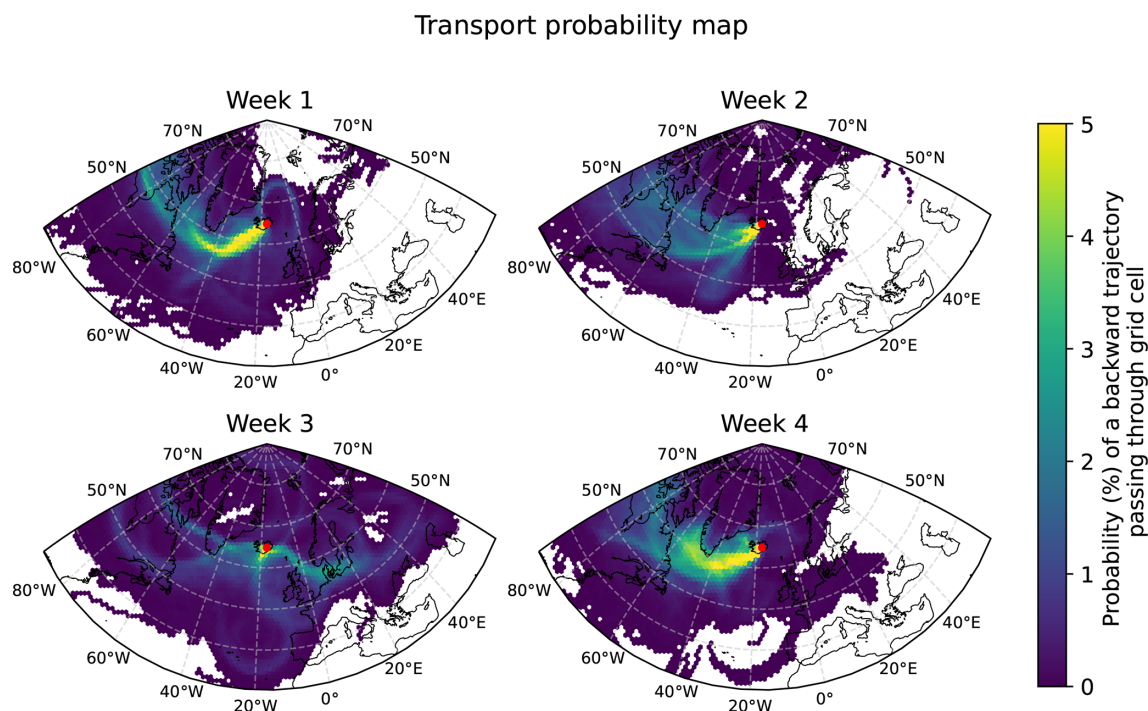


Figure 5. An ensemble of back trajectories was initialised each hour at 2000 m above the Holuhraun eruption site (64.85°N , 16.83°W), as explained in Sect. 2.4. The probability (%) of a backward trajectory passing through a specific grid cell ($A_{i,j}$) is shown here. The start dates of the trajectories are grouped by the weeks of our analysis.

LTS values. The number of outliers with high LTS values implies a contrast in the conditions in the bounding box during the third week. A higher LTS value indicates a strong, low-lying inversion that traps moisture more efficiently in the boundary layer and favours greater cloud cover (Wood and Bretherton, 2006). LTS is calculated as the difference in potential temperature between 720 and 1000 hPa.

Variables affecting the production of sulfate aerosol and the number of aerosols activated to cloud droplets are also shown in Fig. 7. The first box plot shows the ratio of vertical mean gas-phase to aqueous-phase production rate of sulfate aerosol (SO_4^{2-}) inside the plume. The median and quartiles of the ratio have higher values in week 3. A higher ratio indicates either more gas-phase production or less aqueous-phase production of sulfate, which is consistent with the plume location partly covering a region with less cloud during week 3. In the gas-phase, sulfate aerosol is formed through the reaction of SO_2 with OH to form H_2SO_4 vapour. Nucleation and condensation then occur to produce aerosols with a larger size and number. In UKESM1, these gas-phase aerosol processes produce sulfate aerosol in all size modes, whereas in clouds, SO_2 dissolves and undergoes oxidation with H_2O_2 and O_3 to form sulfate (Turnock et al., 2019). The sulfate aerosol produced through in-cloud oxidation is split into the soluble accumulation and coarse modes (Mulcahy et al., 2020). Less aqueous-phase production of sulfate aerosol is therefore in line with the lower values of in-plume soluble ac-

cumulation mode aerosol (i.e. an effective size for droplet nucleation) during week 3. The magnitude of SO_2 emissions in the Holuhraun simulations follow that described in Malavelle et al. (2017) (as shown in their Supplement). Emissions during the first 2 weeks of the eruption were larger than during weeks 3 and 4, which also contributes to the lower amount of soluble accumulation mode aerosol during these weeks in the Holuhraun simulations. However, emissions were still large at an average estimated as $57.5\text{ kt SO}_2\text{ d}^{-1}$ during the latter weeks, and we would expect an aerosol perturbation to N_d in an environment susceptible to aerosol perturbation.

Accumulation mode aerosol dominates the contribution to CCN concentrations over polluted land regions (e.g. Chang et al., 2017). In UKESM1, aerosols are activated into cloud droplets using the activation scheme of Abdul-Razzak and Ghan (2000). Once per time step the activation scheme calculates N_d at cloud base and imposes it on all grid cells above the cloud base within the same liquid cloud. The activation scheme also depends on the subgrid vertical velocity variance (West et al., 2014). The box plots show that although soluble accumulation mode aerosol is lower during the last 2 weeks of September than the first 2 weeks, the difference in the number of activated particles at the lowest cloud base in the bounding region is less evident. In an updraught-limited activation regime that is more likely to occur under polluted air masses (such as week 3), cloud droplet formation is proportional to updraught velocity and essentially independent of

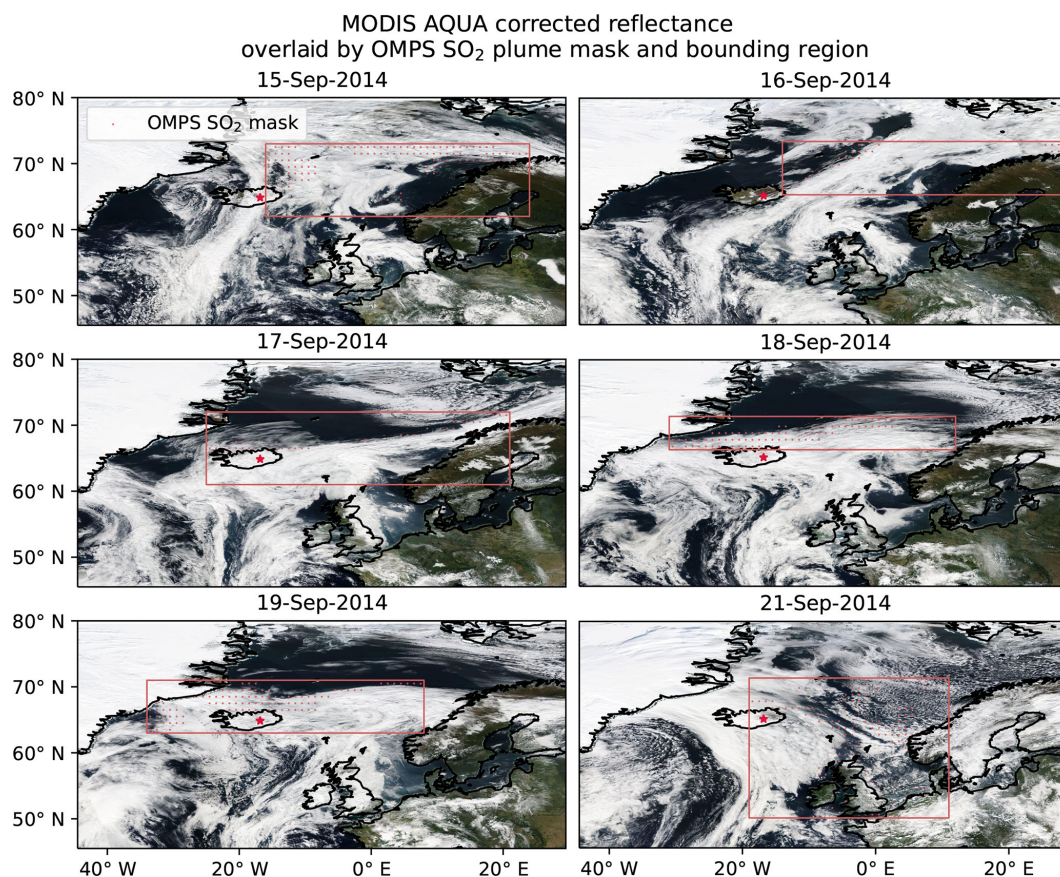


Figure 6. Visible image from MODIS Aqua for 15–21 September 2014. The OMPS SO₂ plume mask and bounding region are overlaid on the visible imagery. The date of 20 September is excluded due to no OMPS SO₂ retrieval on that day. Visible imagery is obtained from the corrected reflectance (true colour) MODIS Aqua data available from NASA Worldview (<https://worldview.earthdata.nasa.gov/>, last access: 1 June 2023).

aerosol number concentration (Reutter et al., 2009). The last 2 weeks of September exhibits larger variance in subgrid vertical velocity at the lowest cloud base. Hence, an updraught-limited regime would explain why week 3 has a similar number of activated particles at the lowest cloud base compared to other weeks despite lower accumulation mode aerosol inside the bounding box. Haghghatnasab et al. (2022) showed how increasing the updraught velocity can increase the background CCN concentration in the Holuhraun domain in a cloud-resolving model. Yet, further study would be needed to definitively identify the activation regime during each week of our study to support these results.

The LWP response to an increase in N_d likely depends on the meteorological conditions present, as noted in the introduction. Our results show a shift in the distribution of MODIS LWP inside the plume during weeks 1, 2 and 4 that results from more values in the range $\sim 100\text{--}300\text{ g m}^{-2}$ and less values $\sim < 100\text{ g m}^{-2}$ inside the plume. An increase in LWP is traditionally associated with reduced collision coalescence in clouds with smaller droplets that can delay the onset of precipitation and result in the accumulation of in-

cloud water content (Pincus and Baker, 1994). LWP has been found to increase in low, precipitating marine liquid clouds below moist air, whereas in thicker, non-precipitating clouds below dry air there may be a decrease in LWP due to an increase in cloud top entrainment (Toll et al., 2019). The simulations show that humid conditions are present during these weeks, and some clouds are likely to be precipitating (indicated by $r_{\text{eff}} > 14\text{ }\mu\text{m}$ as shown in Fig. 3 and Animation S5), which would be in support of conditions favourable for an increase in LWP. However, the in-plume LWPs in the Holuhraun simulation were not significantly greater than the values out-of-plume during weeks 1, 2 and 4, which contrasts with climate models' tendency to produce an unrealistic large increase in LWP when N_d increases (Malavelle et al., 2017; Toll et al., 2019). A weak LWP response to aerosol perturbation in UKESM1-Hol is consistent with results from HadGEM3-UKCA, which is an earlier version of the aerosol–climate model used in this work (Ghan et al., 2016; Zhang et al., 2016; Malavelle et al., 2017). Ghan et al. (2016) hypothesised that the weak LWP response in HadGEM3-UKCA could be partly due to the autoconversion

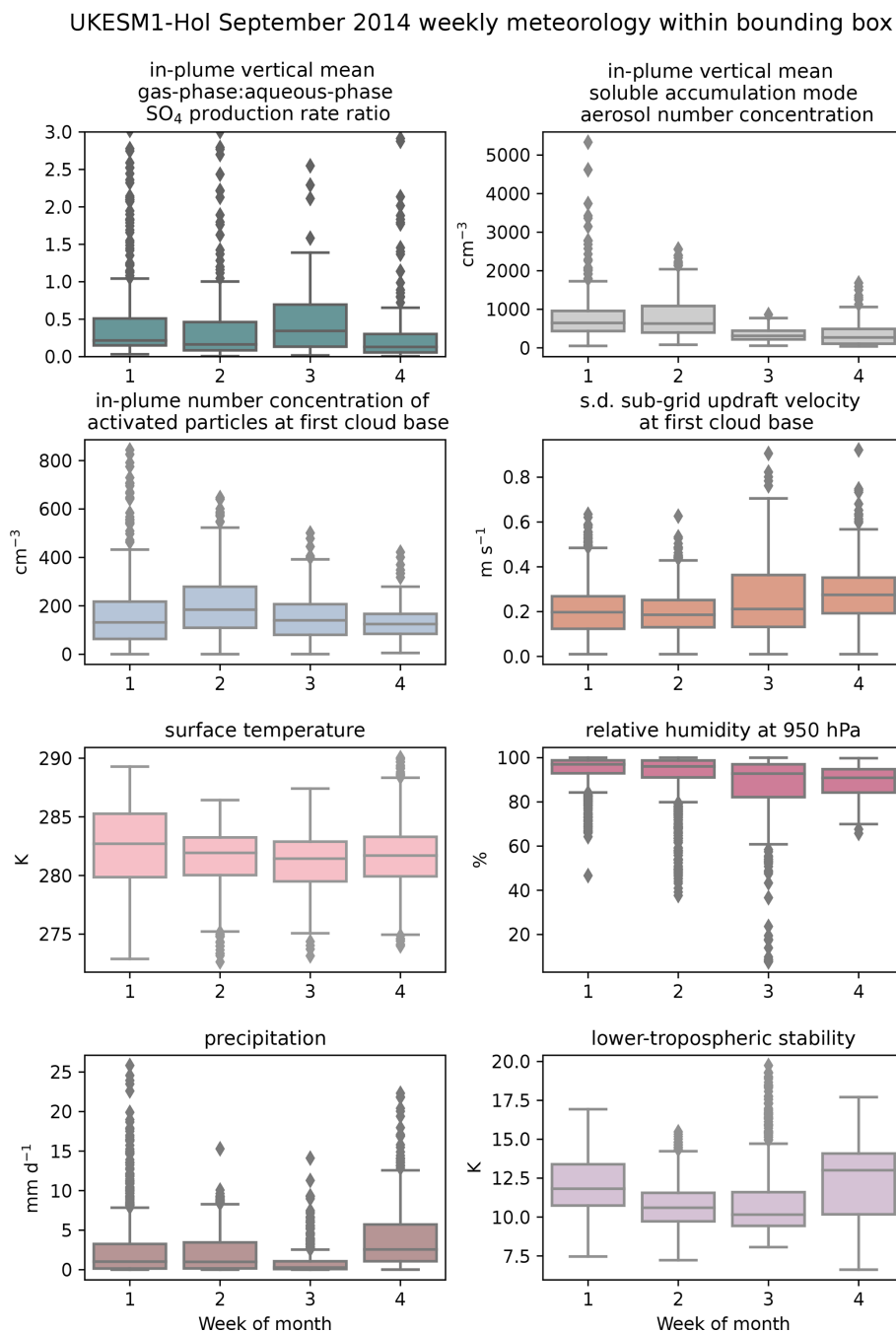


Figure 7. Box plots of UKESM1-Hol meteorological variables within the OMPS plume mask bounding box. The variables shown are ratio of vertical mean gas-phase to aqueous-phase production rate of SO_4 , vertical mean soluble accumulation mode aerosol number concentration, number concentration of activated particles at first cloud base, standard deviation of sub-grid updraft velocity at first cloud base, surface temperature, precipitation, relative humidity at 950 hPa and lower-tropospheric stability. The daily mean data within the bounding box are aggregated into the 4 weeks. The first three box plots show the in-plume values. The y axis of the SO_4 production rate ratio was adjusted to show the box as there were outliers with high values. The box plots show the interquartile range and the median, with the whiskers denoting 1.5 times the interquartile range, and outliers that are defined as being outside this range are shown as diamond points.

scheme used. If instead the meteorological conditions were favourable to the entrainment processes that can decrease LWP, we would not expect a decrease in LWP to be simulated since most current and previous generations of climate models do not include a parameterisation where aerosol can impact cloud top entrainment (Toll et al., 2019). We do not discuss the LWP response in week 3 further here due to the missing causal processes of ACIs.

3.4.3 Limitations of using observed column amount of SO₂ to identify the aerosol plume

In our analyses we use the column amount of SO₂ to track the aerosol plume as this information is readily available from satellite observations and model simulations. We assume that the column amount of SO₂ is a good proxy for where sulfate aerosol is produced, as this information is not observable from satellite observations. Figure S1 shows how the column amount of SO₂ compares to the vertical mean sulfate mass concentration in the UKESM1-Hol simulations. The spatial location of sulfate aerosol is in good agreement with the location of the column amount of SO₂ for our snapshot days. However, the unmasked sulfate mass concentration is elevated across a larger area both inside and outside of the plume mask bounding box. The more widespread enhanced aerosol load revealed by the sulfate mass concentration, in combination with slight differences between the modelled and observed SO₂, is likely why the out-of-plume N_d in the UKESM1-Hol concentration is larger than in the UKESM1-Ctrl. The absolute values of N_d observed by MODIS are lower than in UKESM1-Hol, and the MODIS out-of-plume N_d is comparable to the out-of-plume N_d in UKESM1-Ctrl.

In addition, the OMPS column amount of SO₂ does not provide information on when the sulfate plume is within the cloud layer where the aerosol–cloud perturbation takes place. Therefore, we compare the SO₂ plume height obtained from IASI (Carboni et al., 2016) and the height of the maximum SO₂ mole fraction from the UKESM1-Hol simulations to the liquid cloud height obtained from MODIS Aqua. Animation S8 shows for each day when the SO₂ plume height in the IASI observations and the height of the maximum SO₂ mole fraction in the Holuhraun simulations are below or above the MODIS Aqua liquid cloud top. On most days, there are grid cells within the SO₂ plume that are both above and below the observed liquid cloud top height. Animation S9 shows the vertical mean profile of the UKESM1-Hol SO₂ mole fraction, IASI SO₂ plume height and MODIS liquid cloud top height when averaged over latitude. The MODIS Aqua liquid cloud top height in the latitudinal mean is close to the altitude of maximum SO₂, with SO₂ generally spanning above and below this height. Therefore, we expect the sulfate aerosol produced in the SO₂ plume to be interacting with liquid water clouds. However, isolating when the sulfate aerosol plume is interacting with clouds is difficult to decipher and a limitation of using satellite observations alone.

The analysis of sulfate mass aerosol and SO₂ plume height shows the limitations in identifying an aerosol plume mask for informing satellite–model comparisons. At smaller scales, the near-infrared reflectance observed by MODIS Terra has been used to identify polluted clouds and unpolluted clouds (Trofimov et al., 2020).

4 Discussion and conclusions

Opportunistic experiments with a known aerosol source, such as degassing volcanic eruptions, offer a way to investigate aerosol–cloud interactions (e.g. Christensen et al., 2022). Our study has built on previous analyses of ACIs following the 2014–2015 Holuhraun eruption (McCoy and Hartmann, 2015; Malavelle et al., 2017; Chen et al., 2022; Haghghatnasab et al., 2022). We utilise an in-plume vs. out-of-plume analysis approach to isolate aerosol perturbations to marine cloud properties in satellite observations and UKESM1-A simulations and trajectory modelling to understand the impact of air mass history on ACIs. Particularly we build on the study of Haghghatnasab et al. (2022), who also used a plume analysis approach, but we use a more detailed plume tracking method and extend the plume analysis approach to the rest of September. The extension of the analysis time frame allows us to group our analysis into weeks that experience differing air mass histories and meteorological conditions and elucidate their role in ACIs.

We have shown during the first 2 weeks of September that there is an increase in N_d and decrease in r_{eff} observed and simulated by UKESM1-Hol when the eruption aerosol plume likely interacts with liquid clouds. As expected, the increased N_d and decreased r_{eff} inside the plume are not reproduced in UKESM1-Ctrl, indicating the perturbation is due to ACIs and not differences in meteorology. Our results, which reveal an increase in N_d and decrease in r_{eff} due to the Holuhraun eruption aerosol plume are, in line with previous ACI studies of the eruption (McCoy and Hartmann, 2015; Malavelle et al., 2017; Haghghatnasab et al., 2022; Chen et al., 2022). However, during the third week in September an increase in N_d is neither observed nor modelled. In the fourth week of September, we observe an increase in N_d and decrease in r_{eff} but an insignificant change in the simulations. To understand what caused the different responses of clouds to increased aerosol across the weeks of our analysis, we used trajectory modelling to track the air mass history in the region, alongside assessing the meteorology and activation of aerosols into cloud droplets using the UKESM1-A simulations.

The 10 d back trajectories reveal that air masses arriving at the Holuhraun eruption site during the third week will likely be more polluted than the other weeks due to passing over western Europe rather than originating in pristine regions. Polluted air masses are also more likely to experience updraught-limited rather than aerosol-limited activation into cloud droplets (Reutter et al., 2009). Hence, the

conditions in the third week may be less susceptible to further aerosol-induced increases in N_d than the other weeks of our analysis due to the polluted background (e.g. Jones et al., 1994; Carslaw et al., 2013). The meteorological fields in the UKESM1-Hol simulation show the third week is drier in terms of relative humidity and precipitation, with the satellite imagery indicating a region of persistent clear skies in the north of the bounding box region being the likely cause. The meteorological conditions during the third week therefore support the higher ratio of gas-phase to in-cloud production of sulfate aerosol, which produces less soluble accumulation mode aerosol in the third week, the dominant aerosol mode in the contribution to CCN concentrations over polluted land regions. Overall, we therefore conclude that a combination of the air mass history and background meteorological factors strongly influences aerosol–cloud interactions in the third week. The ability of background N_d and meteorology in the modulation of ACIs illustrates the importance of improving knowledge of background conditions for accurately calculating ACIs. For example, the pre-industrial aerosol loading is a dominant source of uncertainty in present-day aerosol effective radiative forcing (ERF; Carslaw et al., 2013), and present-day analogues to pristine environments can contribute towards constraining aerosol forcing uncertainty (I. L. McCoy et al., 2020; Regayre et al., 2020).

We assessed the LWP response in the 3 weeks where we isolated an observed shift to smaller and more numerous liquid cloud droplets inside the aerosol plume. We find an observed decrease in the likelihood of small LWP values ($< \sim 100 \text{ g m}^{-2}$) and increase in likelihood of LWP values in the range of $\sim 100\text{--}300 \text{ g m}^{-2}$ inside the plume, resulting in a statistically significant increase in in-plume perturbation LWP. While Malavelle et al. (2017) and Chen et al. (2022) did not isolate an observed perturbation to LWP in monthly means, Haghghatnasab et al. (2022) showed an in-plume decrease in the probability of values with low LWP and an increase in values with high LWP in satellite observations and cloud-resolving simulations for the first week, which is consistent with our results. Cloud-resolving simulations of the Holuhraun eruption suggest there is a decrease in light rain and increase in heavy rain during the first week (Haghghatnasab et al., 2022). A decrease in light rain may be due to reduced collision coalescence of smaller droplets that can delay precipitation and lead to droplets growing larger in size before precipitating, increasing heavy rain and shifting the distribution of in-plume LWP values (Fan et al., 2016; Haghghatnasab et al., 2022). This mechanism of an increase in LWP due to precipitation suppression supports our observed increase in LWP values inside the plume during the first 2 weeks of September. However, in UKESM1-Hol, the distribution of LWP values in-plume is not significantly different from that out-of-plume. Malavelle et al. (2017) showed that HadGEM3-UKCA (a previous generation of the aerosol–climate model used in UKESM1) pro-

duced a minimal LWP response following the Holuhraun eruption but that models generally overestimate the increase in LWP due to increased aerosol (Malavelle et al., 2017; Toll et al., 2017).

Chen et al. (2022) showed a significant increase in satellite observation cloud fraction following the Holuhraun eruption when using a machine learning approach that accounts for meteorological confounders. Consistently, our results show an observed increase in cloud fraction during the first 2 weeks of September 2014. In the first week the increase is simulated by the volcanic and control UKESM1 simulations, although the increase in cloud fraction is larger in the volcanic simulation. However, in the second week the simulations show a decrease in cloud fraction. In the fourth week, there is a non-significant decrease in observed cloud fraction but a significant decrease in the model simulations. The similarity in the in-plume perturbation to cloud fraction between the volcanic and control simulations across our analysis indicates much of the simulated cloud fraction change is likely dominated by meteorological covariability. Further simulations would be needed to isolate if the smaller differences between the in-plume perturbation to cloud fraction in the control and Holuhraun simulations could be attributed to aerosols. For example, Grosvenor and Carslaw (2020) examined the contributions of changes in N_d , LWP and cloud fractions to pre-industrial to present-day aerosol ERF in UKESM1-A. Their results showed that LWP and cloud fraction were the dominant terms in the radiative forcing of aerosol–cloud interactions over the North Atlantic and that cloud fraction changes are more dominant in regions of broken cloud. An additional simulation was conducted in the Grosvenor and Carslaw (2020) study where N_d was prevented from modifying rain formation through the autoconversion parameterisation, and in these simulations there was a negligible change in cloud fraction over the North Atlantic.

To conclude, the causal chain of events highlighted over 2 decades ago (e.g. Haywood and Boucher, 2000) of increases in cloud droplet number concentration decreasing cloud effective radius (Twomey, 1974), which delays autoconversion and precipitation processes leading to greater cloud liquid water (Albrecht, 1989), appears to apply in this study. We suggest that ensembles of climate model simulations (e.g. Jordan et al., 2024), higher-resolution nested simulations and a more comprehensive use of a Lagrangian framework (e.g. Coopman et al., 2018) of this opportunistic experiment would provide a more detailed assessment of the causality of meteorological conditions affecting the aerosol perturbation to cloud properties.

Code and data availability. The MODIS cloud products from the MODIS COSP dataset (MCD06COSP_D3_MODIS) and from Aqua (MYD06_L2) used in this study are available from the Atmosphere Archive and Distribution System Distributed Active Archive Center of the National Aeronautics and Space Adminis-

tration (LAADS-DAAC, NASA) (https://doi.org/10.5067/MODIS/MCD06COSP_D3_MODIS.062, NASA, 2022; Pincus et al., 2023, and https://doi.org/10.5067/MODIS/MYD06_L2.061, Platnick et al., 2015). The OMPS SO₂ (OMPS_NPP_NMSO2_PLCL2 v2) data used in this study are available to download from Goddard Earth Sciences Data and Information Services Center (GES-DISC, NASA) (<https://doi.org/10.5067/MEASURES/SO2/DATA205>, Li et al., 2020a). Simplified data and code required to reproduce the main figures in this article are provided on Zenodo (<https://doi.org/10.5281/zenodo.12664100>; Peace et al., 2024). All other underlying datasets generated and/or analysed during the current study are available from the corresponding author upon reasonable request.

Supplement. The supplement related to this article is available online at: <https://doi.org/10.5194/acp-24-9533-2024-supplement>.

Author contributions. AHP and JMH designed the study. Gridded MODIS Aqua data were created from Level 2 products by YC. GJ ran the model simulations. ED and DGP provided guidance in the use of HYSPLIT trajectories. Data analysis and figure preparation were completed by AHP. All co-authors discussed and interpreted the results. AHP wrote the manuscript with advice from all co-authors.

Competing interests. The contact author has declared that none of the authors has any competing interests.

Disclaimer. Publisher's note: Copernicus Publications remains neutral with regard to jurisdictional claims made in the text, published maps, institutional affiliations, or any other geographical representation in this paper. While Copernicus Publications makes every effort to include appropriate place names, the final responsibility lies with the authors.

Acknowledgements. Daniel G. Partridge would like to express his gratitude to Zak Kipling for providing support in obtaining HYSPLIT input files from ERA-Interim reanalysis data. We would like to thank Paul Kim who helped develop the running and plotting framework for HYSPLIT trajectories and Andy Jones for helping with the experimental set-up of UKESM1. We acknowledge the use of imagery from the NASA Worldview application (<https://worldview.earthdata.nasa.gov>, last access: 1 June 2023), part of the NASA Earth Observing System Data and Information System (EOSDIS).

Financial support. This research has been supported by the NERC ADVANCE grant (NE/S015671/1), the European Union's Horizon 2020 research and innovation programme under the CON-STRAIN grant agreement 820829, and the Met Office Hadley Centre Climate Programme funded by BEIS.

Review statement. This paper was edited by Matthias Tesche and reviewed by two anonymous referees.

References

- Abdul-Razzak, H. and Ghan, S. J.: A parameterization of aerosol activation: 2. Multiple aerosol types, *J. Geophys. Res.-Atmos.*, 105, 6837–6844, <https://doi.org/10.1029/1999JD901161>, 2000.
- Ackerman, A. S., Kirkpatrick, M. P., Stevens, D. E., and Toon, O. B.: The impact of humidity above stratiform clouds on indirect aerosol climate forcing, *Nature*, 432, 1014–1017, <https://doi.org/10.1038/nature03174>, 2004.
- Albrecht, B. A.: Aerosols, Cloud Microphysics, and Fractional Cloudiness, *Science*, 245, 1227–1230, <https://doi.org/10.1126/science.245.4923.1227>, 1989.
- Andreae, M. O., Jones, C. D., and Cox, P. M.: Strong present-day aerosol cooling implies a hot future, *Nature*, 435, 1187–1190, <https://doi.org/10.1038/nature03671>, 2005.
- Archibald, A. T., O'Connor, F. M., Abraham, N. L., Archer-Nicholls, S., Chipperfield, M. P., Dalvi, M., Folberth, G. A., Dennis, F., Dhomse, S. S., Griffiths, P. T., Hardacre, C., Hewitt, A. J., Hill, R. S., Johnson, C. E., Keeble, J., Köhler, M. O., Morgenstern, O., Mulcahy, J. P., Ordóñez, C., Pope, R. J., Rumbold, S. T., Russo, M. R., Savage, N. H., Sellar, A., Stringer, M., Turnock, S. T., Wild, O., and Zeng, G.: Description and evaluation of the UKCA stratosphere–troposphere chemistry scheme (Strat-Trop v1.0) implemented in UKESM1, *Geosci. Model Dev.*, 13, 1223–1266, <https://doi.org/10.5194/gmd-13-1223-2020>, 2020.
- Bellouin, N., Quaas, J., Gryspeerdt, E., Kinne, S., Stier, P., Watson-Parris, D., Boucher, O., Carslaw, K. S., Christensen, M., Daniou, A.-L., Dufresne, J.-L., Feingold, G., Fiedler, S., Forster, P., Gettelman, A., Haywood, J. M., Lohmann, U., Malavelle, F., Mauritsen, T., McCoy, D. T., Myhre, G., Mülmenstädt, J., Neubauer, D., Possner, A., Rugenstein, M., Sato, Y., Schulz, M., Schwartz, S. E., Sourdeval, O., Storelvmo, T., Toll, V., Winker, D., and Stevens, B.: Bounding Global Aerosol Radiative Forcing of Climate Change, *Rev. Geophys.*, 58, e2019RG000660, <https://doi.org/10.1029/2019RG000660>, 2020.
- Bodas-Salcedo, A., Webb, M. J., Bony, S., Chepfer, H., Dufresne, J.-L., Klein, S. A., Zhang, Y., Marchand, R., Haynes, J. M., Pincus, R., and John, V. O.: COSP: Satellite simulation software for model assessment, *B. Am. Meteorol. Soc.*, 92, 1023–1043, <https://doi.org/10.1175/2011BAMS2856.1>, 2011.
- Boichu, M., Chiapello, I., Brogniez, C., Péré, J.-C., Thieuleux, F., Torres, B., Blarel, L., Mortier, A., Podvin, T., Goloub, P., Söhne, N., Clarisse, L., Bauduin, S., Hendrick, F., Theys, N., Van Roozendaal, M., and Tanré, D.: Current challenges in modelling far-range air pollution induced by the 2014–2015 Bárðarbunga fissure eruption (Iceland), *Atmos. Chem. Phys.*, 16, 10831–10845, <https://doi.org/10.5194/acp-16-10831-2016>, 2016.
- Boutle, I. A., Abel, S. J., Hill, P. G., and Morcrette, C. J.: Spatial variability of liquid cloud and rain: Observations and microphysical effects, *Q. J. Roy. Meteor. Soc.*, 140, 583–594, <https://doi.org/10.1002/qj.2140>, 2014.
- Bréon, F.-M., Tanré, D., and Generoso, S.: Aerosol Effect on Cloud Droplet Size Monitored from Satellite, *Science*, 295, 834–838, <https://doi.org/10.1126/science.1066434>, 2002.
- Bretherton, C. S., Blossey, P. N., and Uchida, J.: Cloud droplet sedimentation, entrainment efficiency, and subtropi-

- cal stratocumulus albedo, *Geophys. Res. Lett.*, 34, L03813, <https://doi.org/10.1029/2006GL027648>, 2007.
- Carboni, E., Grainger, R., Walker, J., Dudhia, A., and Siddans, R.: A new scheme for sulphur dioxide retrieval from IASI measurements: application to the Eyjafjallajökull eruption of April and May 2010, *Atmos. Chem. Phys.*, 12, 11417–11434, <https://doi.org/10.5194/acp-12-11417-2012>, 2012.
- Carboni, E., Grainger, R. G., Mather, T. A., Pyle, D. M., Thomas, G. E., Siddans, R., Smith, A. J. A., Dudhia, A., Koukouli, M. E., and Balis, D.: The vertical distribution of volcanic SO₂ plumes measured by IASI, *Atmos. Chem. Phys.*, 16, 4343–4367, <https://doi.org/10.5194/acp-16-4343-2016>, 2016.
- Carboni, E., Mather, T. A., Schmidt, A., Grainger, R. G., Pfeiffer, M. A., Ialongo, I., and Theys, N.: Satellite-derived sulfur dioxide (SO₂) emissions from the 2014–2015 Holuhraun eruption (Iceland), *Atmos. Chem. Phys.*, 19, 4851–4862, <https://doi.org/10.5194/acp-19-4851-2019>, 2019.
- Carslaw, K. S., Lee, L. A., Reddington, C. L., Pringle, K. J., Rap, A., Forster, P. M., Mann, G. W., Spracklen, D. V., Woodhouse, M. T., Regayre, L. A., and Pierce, J. R.: Large contribution of natural aerosols to uncertainty in indirect forcing, *Nature*, 503, 67–71, <https://doi.org/10.1038/nature12674>, 2013.
- Chang, D. Y., Lelieveld, J., Tost, H., Steil, B., Pozzer, A., and Yoon, J.: Aerosol physicochemical effects on CCN activation simulated with the chemistry–climate model EMAC, *Atmos. Environ.*, 162, 127–140, <https://doi.org/10.1016/j.atmosenv.2017.03.036>, 2017.
- Chen, Y., Haywood, J., Wang, Y., Malavelle, F., Jordan, G., Partridge, D., Fieldsend, J., De Leeuw, J., Schmidt, A., Cho, N., Oreopoulos, L., Platnick, S., Grosvenor, D., Field, P., and Lohmann, U.: Machine learning reveals climate forcing from aerosols is dominated by increased cloud cover, *Nat. Geosci.*, 15, 609–614, <https://doi.org/10.1038/s41561-022-00991-6>, 2022.
- Christensen, M. W., Gettelman, A., Cermak, J., Dagan, G., Diamond, M., Douglas, A., Feingold, G., Glassmeier, F., Goren, T., Grosvenor, D. P., Gryspeerd, E., Kahn, R., Li, Z., Ma, P.-L., Malavelle, F., McCoy, I. L., McCoy, D. T., McFarquhar, G., Mühlenthal, J., Pal, S., Possner, A., Povey, A., Quaas, J., Rosenfeld, D., Schmidt, A., Schrödner, R., Sorooshian, A., Stier, P., Toll, V., Watson-Parris, D., Wood, R., Yang, M., and Yuan, T.: Opportunistic experiments to constrain aerosol effective radiative forcing, *Atmos. Chem. Phys.*, 22, 641–674, <https://doi.org/10.5194/acp-22-641-2022>, 2022.
- Coopman, Q., Garrett, T. J., Finch, D. P., and Riedi, J.: High Sensitivity of Arctic Liquid Clouds to Long-Range Anthropogenic Aerosol Transport, *Geophys. Res. Lett.*, 45, 372–381, <https://doi.org/10.1002/2017GL075795>, 2018.
- Dee, D. P., Uppala, S. M., Simmons, A. J., Berrisford, P., Poli, P., Kobayashi, S., Andrae, U., Balmaseda, M. A., Balsamo, G., Bauer, P., Bechtold, P., Beljaars, A. C. M., van de Berg, L., Bidlot, J., Bormann, N., Delsol, C., Dragani, R., Fuentes, M., Geer, A. J., Haimberger, L., Healy, S. B., Hersbach, H., Hólm, E. V., Isaksen, I., Kållberg, P., Köhler, M., Matricardi, M., McNally, A. P., Monge-Sanz, B. M., Morcrette, J.-J., Park, B.-K., Peubey, C., de Rosnay, P., Tavalato, C., Thépaut, J.-N., and Vitart, F.: The ERA-Interim reanalysis: configuration and performance of the data assimilation system, *Q. J. Roy. Meteor. Soc.*, 137, 553–597, <https://doi.org/10.1002/qj.828>, 2011.
- Douville, H., Raghavan, K., Renwick, J., Allan, R. P., Arias, P. A., Barlow, M., Cerezo-Mota, R., Cherchi, A., Gan, T. Y., Gergis, J., Jiang, D., Khan, A., Pokam Mba, W., Rosenfeld, D., Tierney, J., and Zolina, O.: Water Cycle Changes, in: *Climate Change 2021: The Physical Science Basis. Contribution of Working Group I to the Sixth Assessment Report of the Intergovernmental Panel on Climate Change*, edited by: Masson-Delmotte, V., Zhai, P., Pirani, A., Connors, S. L., Péan, C., Berger, S., Caud, N., Chen, Y., Goldfarb, L., Gomis, M. I., Huang, M., Leitzell, K., Lonnoy, E., Matthews, J. B. R., Maycock, T. K., Waterfield, T., Yelekçi, O., Yu, R., and Zhou, B., Cambridge University Press, Cambridge, United Kingdom and New York, NY, USA, 1055–1210, <https://doi.org/10.1017/9781009157896.010>, 2021.
- Eyring, V., Bony, S., Meehl, G. A., Senior, C. A., Stevens, B., Stouffer, R. J., and Taylor, K. E.: Overview of the Coupled Model Intercomparison Project Phase 6 (CMIP6) experimental design and organization, *Geosci. Model Dev.*, 9, 1937–1958, <https://doi.org/10.5194/gmd-9-1937-2016>, 2016.
- Eyring, V., Gillett, N. P., Achuta Rao, K. M., Barimalala, R., Barreiro Parrillo, M., Bellouin, N., Cassou, C., Durack, P. J., Kosaka, Y., McGregor, S., Min, S., Morgenstern, O., and Sun, Y.: Human Influence on the Climate System, in: *Climate Change 2021: The Physical Science Basis. Contribution of Working Group I to the Sixth Assessment Report of the Intergovernmental Panel on Climate Change*, edited by: Masson-Delmotte, V., Zhai, P., Pirani, A., Connors, S. L., Péan, C., Berger, S., Caud, N., Chen, Y., Goldfarb, L., Gomis, M. I., Huang, M., Leitzell, K., Lonnoy, E., Matthews, J. B. R., Maycock, T. K., Waterfield, T., Yelekçi, O., Yu, R., and Zhou, B., Cambridge University Press, Cambridge, United Kingdom and New York, NY, USA, 423–552, <https://doi.org/10.1017/9781009157896.005>, 2021.
- Fan, J., Wang, Y., Rosenfeld, D., and Liu, X.: Review of Aerosol–Cloud Interactions: Mechanisms, Significance, and Challenges, *J. Atmos. Sci.*, 73, 4221–4252, <https://doi.org/10.1175/JAS-D-16-0037.1>, 2016.
- Feingold, G., Eberhard, W. L., Veron, D. E., and Previdi, M.: First measurements of the Twomey indirect effect using ground-based remote sensors, *Geophys. Res. Lett.*, 30, 1287, <https://doi.org/10.1029/2002GL016633>, 2003.
- Flynn, L., Long, C., Wu, X., Evans, R., Beck, C. T., Petropavlovskikh, I., McConville, G., Yu, W., Zhang, Z., Niu, J., Beach, E., Hao, Y., Pan, C., Sen, B., Novicki, M., Zhou, S., and Seftor, C.: Performance of the Ozone Mapping and Profiler Suite (OMPS) products, *J. Geophys. Res.-Atmos.*, 119, 6181–6195, <https://doi.org/10.1002/2013JD020467>, 2014.
- Forster, P., Storelvmo, T., Armour, K., Collins, W., Dufresne, J.-L., Frame, D., Lunt, D. J., Mauritsen, T., Palmer, M. D., Watanabe, M., Wild, M., and Zhang, H.: The Earth’s Energy Budget, Climate Feedbacks, and Climate Sensitivity, in: *Climate Change 2021: The Physical Science Basis. Contribution of Working Group I to the Sixth Assessment Report of the Intergovernmental Panel on Climate Change*, edited by: Masson-Delmotte, V., Zhai, P., Pirani, A., Connors, S. L., Péan, C., Berger, S., Caud, N., Chen, Y., Goldfarb, L., Gomis, M. I., Huang, M., Leitzell, K., Lonnoy, E., Matthews, J. B. R., Maycock, T. K., Waterfield, T., Yelekçi, O., Yu, R., and Zhou, B., Cambridge University Press, Cambridge, United Kingdom and New York, NY, USA, 923–1054, <https://doi.org/10.1017/9781009157896.009>, 2021.
- Ghan, S. J., Wang, M., Zhang, S., Ferrachat, S., Gettelman, A., Griesfeller, J., Kipling, Z., Lohmann, U., Morrison, H., Neubauer, D., Partridge, D. G., Stier, P., Takemura, T., Wang,

- H., and Zhang, K.: Challenges in constraining anthropogenic aerosol effects on cloud radiative forcing using present-day spatiotemporal variability, *P. Natl. Acad. Sci. USA*, 113, 5804–5811, <https://doi.org/10.1073/pnas.1514036113>, 2016.
- Grosvenor, D. P. and Carslaw, K. S.: The decomposition of cloud–aerosol forcing in the UK Earth System Model (UKESM1), *Atmos. Chem. Phys.*, 20, 15681–15724, <https://doi.org/10.5194/acp-20-15681-2020>, 2020.
- Gryspeerdt, E., Goren, T., Sourdeval, O., Quaas, J., Mülmenstädt, J., Dipu, S., Unglaub, C., Gettelman, A., and Christensen, M.: Constraining the aerosol influence on cloud liquid water path, *Atmos. Chem. Phys.*, 19, 5331–5347, <https://doi.org/10.5194/acp-19-5331-2019>, 2019.
- Gryspeerdt, E., McCoy, D. T., Crosbie, E., Moore, R. H., Nott, G. J., Painemal, D., Small-Griswold, J., Sorooshian, A., and Ziemba, L.: The impact of sampling strategy on the cloud droplet number concentration estimated from satellite data, *Atmos. Meas. Tech.*, 15, 3875–3892, <https://doi.org/10.5194/amt-15-3875-2022>, 2022.
- Haghighatnasab, M., Kretzschmar, J., Block, K., and Quaas, J.: Impact of Holuhraun volcano aerosols on clouds in cloud-system-resolving simulations, *Atmos. Chem. Phys.*, 22, 8457–8472, <https://doi.org/10.5194/acp-22-8457-2022>, 2022.
- Haywood, J. and Boucher, O.: Estimates of the direct and indirect radiative forcing due to tropospheric aerosols: A review, *Rev. Geophys.*, 38, 513–543, <https://doi.org/10.1029/1999RG000078>, 2000.
- Haywood, J. M., Jones, A., Clarisse, L., Bourassa, A., Barnes, J., Telford, P., Bellouin, N., Boucher, O., Agnew, P., Clerbaux, C., Coheur, P., Degenstein, D., and Braesicke, P.: Observations of the eruption of the Sarychev volcano and simulations using the HadGEM2 climate model, *J. Geophys. Res.-Atmos.*, 115, D21212, <https://doi.org/10.1029/2010JD014447>, 2010.
- Ialongo, I., Hakkarainen, J., Kivi, R., Anttila, P., Krotkov, N. A., Yang, K., Li, C., Tukiainen, S., Hassinen, S., and Tamminen, J.: Comparison of operational satellite SO₂ products with ground-based observations in northern Finland during the Icelandic Holuhraun fissure eruption, *Atmos. Meas. Tech.*, 8, 2279–2289, <https://doi.org/10.5194/amt-8-2279-2015>, 2015.
- Ilyinskaya, E., Schmidt, A., Mather, T. A., Pope, F. D., Witham, C., Baxter, P., Jóhannsson, T., Pfeffer, M., Barsotti, S., Singh, A., Sanderson, P., Bergsson, B., McCormick Kilbride, B., Donovan, A., Peters, N., Oppenheimer, C., and Edmonds, M.: Understanding the environmental impacts of large fissure eruptions: Aerosol and gas emissions from the 2014–2015 Holuhraun eruption (Iceland), *Earth Planet. Sc. Lett.*, 472, 309–322, <https://doi.org/10.1016/j.epsl.2017.05.025>, 2017.
- Jones, A., Roberts, D. L., and Slingo, A.: A climate model study of indirect radiative forcing by anthropogenic sulphate aerosols, *Nature*, 370, 450–453, <https://doi.org/10.1038/370450a0>, 1994.
- Jones, A., Roberts, D. L., Woodage, M. J., and Johnson, C. E.: Indirect sulphate forcing in a climate model with an interactive sulphur cycle, *J. Geophys. Res.*, 106, 20293–20310, <https://doi.org/10.1029/2000JD000089>, 2001.
- Jordan, G., Malavelle, F., Chen, Y., Peace, A., Duncan, E., Partridge, D. G., Kim, P., Watson-Parris, D., Takemura, T., Neubauer, D., Myhre, G., Skeie, R., Laakso, A., and Haywood, J.: How well are aerosol–cloud interactions represented in climate models? – Part 1: Understanding the sulfate aerosol production from the 2014–15 Holuhraun eruption, *Atmos. Chem. Phys.*, 24, 1939–1960, <https://doi.org/10.5194/acp-24-1939-2024>, 2024.
- Khairoutdinov, M. F. and Kogan, Y. L.: A new cloud physics parameterization in a large-eddy simulation model of marine stratocumulus, *Mon. Weather Rev.*, 128, 229–243, [https://doi.org/10.1175/1520-0493\(2000\)128<0229:ANCPPI>2.0.CO;2](https://doi.org/10.1175/1520-0493(2000)128<0229:ANCPPI>2.0.CO;2), 2000.
- Kuhlbrodt, T., Jones, C. G., Sellar, A., Storkey, D., Blockley, E., Stringer, M., Hill, R., Graham, T., Ridley, J., Blaker, A., Calvert, D., Copsey, D., Ellis, R., Hewitt, H., Hyder, P., Ineson, S., Mulcahy, J., Siahann, A., and Walton, J.: The Low-Resolution Version of HadGEM3 GC3.1: Development and Evaluation for Global Climate, *J. Adv. Model. Earth Sy.*, 10, 2865–2888, <https://doi.org/10.1029/2018MS001370>, 2018.
- Li, C., Krotkov, N. A., Carn, S., Zhang, Y., Spurr, R. J. D., and Joiner, J.: New-generation NASA Aura Ozone Monitoring Instrument (OMI) volcanic SO₂ dataset: algorithm description, initial results, and continuation with the Suomi-NPP Ozone Mapping and Profiler Suite (OMPS), *Atmos. Meas. Tech.*, 10, 445–458, <https://doi.org/10.5194/amt-10-445-2017>, 2017.
- Li, C., Krotkov, N. A., Leonard, P., and Joiner, J.: OMPS/NPP PCA SO₂ Total Column 1-Orbit L2 Swath 50x50km V2, GES DISC [data set], https://doi.org/10.5067/MEASURES/SO2/DATA205_2020a.
- Li, C., Krotkov, N. A., Leonard, P. J. T., Carn, S., Joiner, J., Spurr, R. J. D., and Vasilkov, A.: Version 2 Ozone Monitoring Instrument SO₂ product (OMSO2 V2): new anthropogenic SO₂ vertical column density dataset, *Atmos. Meas. Tech.*, 13, 6175–6191, <https://doi.org/10.5194/amt-13-6175-2020>, 2020b.
- Malavelle, F. F., Haywood, J. M., Jones, A., Gettelman, A., Clarisse, L., Bauduin, S., Allan, R. P., Karset, I. H. H., Kristjánsson, J. E., Oreopoulos, L., Cho, N., Lee, D., Bellouin, N., Boucher, O., Grosvenor, D. P., Carslaw, K. S., Dhomse, S., Mann, G. W., Schmidt, A., Coe, H., Hartley, M. E., Dalvi, M., Hill, A. A., Johnson, B. T., Johnson, C. E., Knight, J. R., O'Connor, F. M., Partridge, D. G., Stier, P., Myhre, G., Platnick, S., Stephens, G. L., Takahashi, H., and Thordarson, T.: Strong constraints on aerosol–cloud interactions from volcanic eruptions, *Nature*, 546, 485–491, <https://doi.org/10.1038/nature22974>, 2017.
- Mann, G. W., Carslaw, K. S., Spracklen, D. V., Ridley, D. A., Manktelow, P. T., Chipperfield, M. P., Pickering, S. J., and Johnson, C. E.: Description and evaluation of GLOMAP-mode: a modal global aerosol microphysics model for the UKCA composition-climate model, *Geosci. Model Dev.*, 3, 519–551, <https://doi.org/10.5194/gmd-3-519-2010>, 2010.
- Mann, H. B. and Whitney, D. R.: On a Test of Whether one of Two Random Variables is Stochastically Larger than the Other, *Ann. Math. Stat.*, 18, 50–60, <https://doi.org/10.1214/aoms/1177730491>, 1947.
- McCoy, D. T. and Hartmann, D. L.: Observations of a substantial cloud-aerosol indirect effect during the 2014–2015 Bárðarbunga-Veiðivötn fissure eruption in Iceland, *Geophys. Res. Lett.*, 42, 10409–10414, <https://doi.org/10.1002/2015GL067070>, 2015.
- McCoy, D. T., Field, P., Gordon, H., Elsaesser, G. S., and Grosvenor, D. P.: Untangling causality in midlatitude aerosol–cloud adjustments, *Atmos. Chem. Phys.*, 20, 4085–4103, <https://doi.org/10.5194/acp-20-4085-2020>, 2020.
- McCoy, I. L., McCoy, D. T., Wood, R., Regayre, L., Watson-Parris, D., Grosvenor, D. P., Mulcahy, J. P., Hu, Y., Bender, F. A.-

- M., Field, P. R., Carslaw, K. S., and Gordon, H.: The hemispheric contrast in cloud microphysical properties constrains aerosol forcing, *P. Natl. Acad. Sci. USA*, 117, 18998–19006, <https://doi.org/10.1073/pnas.1922502117>, 2020.
- Morcrette, C. J.: Improvements to a prognostic cloud scheme through changes to its cloud erosion parametrization, *Atmos. Sci. Lett.*, 13, 95–102, <https://doi.org/10.1002/asl.374>, 2012.
- Mulcahy, J. P., Johnson, C., Jones, C. G., Povey, A. C., Scott, C. E., Sellar, A., Turnock, S. T., Woodhouse, M. T., Abraham, N. L., Andrews, M. B., Bellouin, N., Browse, J., Carslaw, K. S., Dalvi, M., Folberth, G. A., Glover, M., Grosvenor, D. P., Hardacre, C., Hill, R., Johnson, B., Jones, A., Kipling, Z., Mann, G., Mollard, J., O'Connor, F. M., Palmiéri, J., Reddington, C., Rumbold, S. T., Richardson, M., Schutgens, N. A. J., Stier, P., Stringer, M., Tang, Y., Walton, J., Woodward, S., and Yool, A.: Description and evaluation of aerosol in UKESM1 and HadGEM3-GC3.1 CMIP6 historical simulations, *Geosci. Model Dev.*, 13, 6383–6423, <https://doi.org/10.5194/gmd-13-6383-2020>, 2020.
- NASA: MCD06COSP_D3_MODIS – MODIS (Aqua/Terra) Cloud Properties Level 3 daily, 1x1 degree grid, EarthData [data set], https://doi.org/10.5067/MODIS/MCD06COSP_D3_MODIS.062, 2022.
- Peace, A. H., Carslaw, K. S., Lee, L. A., Regayre, L. A., Booth, B. B. B., Johnson, J. S., and Bernie, D.: Effect of aerosol radiative forcing uncertainty on projected exceedance year of a 1.5 °C global temperature rise, *Environ. Res. Lett.*, 15, 0940a6, <https://doi.org/10.1088/1748-9326/aba20c>, 2020.
- Peace, A. H., Chen, Y., Jordan, G., Partridge, D. G., Malavelle, F., Duncan, E., and Haywood, J. M.: In-plume and out-of-plume analysis of aerosol-cloud interactions derived from the 2014–15 Holuhraun volcanic eruption, Zenodo [data set], <https://doi.org/10.5281/zenodo.12664100>, 2024.
- Pfeffer, M. A., Bergsson, B., Barsotti, S., Stefánssdóttir, G., Galle, B., Arellano, S., Conde, V., Donovan, A., Ilyinskaya, E., Burton, M., Aiuppa, A., Whitty, R. C. W., Simmons, I. C., Arason, Þ., Jónasdóttir, E. B., Keller, N. S., Yeo, R. F., Arngrímsson, H., Jóhannsson, Þ., Butwin, M. K., Askew, R. A., Dumont, S., Von Löwis, S., Ingvarsson, Þ., La Spina, A., Thomas, H., Prata, F., Grassa, F., Giudice, G., Stefánsson, A., Marzano, F., Montopoli, M., and Mereu, L.: Ground-Based Measurements of the 2014–2015 Holuhraun Volcanic Cloud (Iceland), *Geosciences*, 8, 29, <https://doi.org/10.3390/geosciences8010029>, 2018.
- Pincus, R. and Baker, M. B.: Effect of precipitation on the albedo susceptibility of clouds in the marine boundary layer, *Nature*, 372, 250–252, <https://doi.org/10.1038/372250a0>, 1994.
- Pincus, R., Platnick, S., Ackerman, S. A., Hemler, R. S., and Patrick Hofmann, R. J.: Reconciling Simulated and Observed Views of Clouds: MODIS, ISCCP, and the Limits of Instrument Simulators, *J. Climate*, 25, 4699–4720, <https://doi.org/10.1175/JCLI-D-11-00267.1>, 2012.
- Pincus, R., Hubanks, P. A., Platnick, S., Meyer, K., Holz, R. E., Botambekov, D., and Wall, C. J.: Updated observations of clouds by MODIS for global model assessment, *Earth Syst. Sci. Data*, 15, 2483–2497, <https://doi.org/10.5194/essd-15-2483-2023>, 2023.
- Platnick, S., Ackerman, S. A., King, M. D., Meyer, K., Menzel, W. P., Holz, R. E., Baum, B. A., and Yang, P.: MYD06_L2 MYD06_L2 MODIS/Aqua Clouds 5-Min L2 Swath 1km and 5km, EarthData [data set], https://doi.org/10.5067/MODIS/MYD06_L2.061, 2015.
- Platnick, S., Meyer, K. G., King, M. D., Wind, G., Amarasinghe, N., Marchant, B., Arnold, G. T., Zhang, Z., Hubanks, P. A., Holz, R. E., Yang, P., Ridgway, W. L., and Riedi, J.: The MODIS cloud optical and microphysical products: Collection 6 updates and examples from Terra and Aqua, *IEEE T. Geosci. Remote*, 55, 502–525, <https://doi.org/10.1109/TGRS.2016.2610522>, 2017.
- Quaas, J., Boucher, O., and Lohmann, U.: Constraining the total aerosol indirect effect in the LMDZ and ECHAM4 GCMs using MODIS satellite data, *Atmos. Chem. Phys.*, 6, 947–955, <https://doi.org/10.5194/acp-6-947-2006>, 2006.
- Rao, S., Klimont, Z., Smith, S. J., Van Dingenen, R., Dentener, F., Bouwman, L., Riahi, K., Amann, M., Bodirsky, B. L., van Vuuren, D. P., Aleluia Reis, L., Calvin, K., Drouet, L., Fricko, O., Fujimori, S., Gernaat, D., Havlik, P., Harmsen, M., Hasegawa, T., Heyes, C., Hilaire, J., Luderer, G., Masui, T., Stehfest, E., Strefler, J., van der Sluis, S., and Tavoni, M.: Future air pollution in the Shared Socio-economic Pathways, *Global Environ. Chang.*, 42, 346–358, <https://doi.org/10.1016/j.gloenvcha.2016.05.012>, 2017.
- Rayner, N. A., Parker, D. E., Horton, E. B., Folland, C. K., Alexander, L. V., Rowell, D. P., Kent, E. C., and Kaplan, A.: Global analyses of sea surface temperature, sea ice, and night marine air temperature since the late nineteenth century, *J. Geophys. Res.-Atmos.*, 108, 4407, <https://doi.org/10.1029/2002JD002670>, 2003.
- Regayre, L. A., Schmale, J., Johnson, J. S., Tatzelt, C., Baccharini, A., Henning, S., Yoshioka, M., Stratmann, F., Gysel-Beer, M., Grosvenor, D. P., and Carslaw, K. S.: The value of remote marine aerosol measurements for constraining radiative forcing uncertainty, *Atmos. Chem. Phys.*, 20, 10063–10072, <https://doi.org/10.5194/acp-20-10063-2020>, 2020.
- Reutter, P., Su, H., Trentmann, J., Simmel, M., Rose, D., Gunthe, S. S., Wernli, H., Andreae, M. O., and Pöschl, U.: Aerosol- and updraft-limited regimes of cloud droplet formation: influence of particle number, size and hygroscopicity on the activation of cloud condensation nuclei (CCN), *Atmos. Chem. Phys.*, 9, 7067–7080, <https://doi.org/10.5194/acp-9-7067-2009>, 2009.
- Schmidt, A., Leadbetter, S., Theys, N., Carboni, E., Witham, C. S., Stevenson, J. A., Birch, C. E., Thordarson, T., Turnock, S., Barsotti, S., Delaney, L., Feng, W., Grainger, R. G., Hort, M. C., Höskuldsson, Á., Ialongo, I., Ilyinskaya, E., Jóhannsson, T., Kenny, P., Mather, T. A., Richards, N. A. D., and Shepherd, J.: Satellite detection, long-range transport, and air quality impacts of volcanic sulfur dioxide from the 2014–2015 flood lava eruption at Bárðarbunga (Iceland), *J. Geophys. Res.-Atmos.*, 120, 9739–9757, <https://doi.org/10.1002/2015JD023638>, 2015.
- Seftor, C. J., Jaross, G., Kowitt, M., Haken, M., Li, J., and Flynn, L. E.: Postlaunch performance of the Suomi National Polar-orbiting Partnership Ozone Mapping and Profiler Suite (OMPS) nadir sensors, *J. Geophys. Res.-Atmos.*, 119, 4413–4428, <https://doi.org/10.1002/2013JD020472>, 2014.
- Seinfeld, J. H., Bretherton, C., Carslaw, K. S., Coe, H., DeMott, P. J., Dunlea, E. J., Feingold, G., Ghan, S., Guenther, A. B., Kahn, R., Kraucunas, I., Kreidenweis, S. M., Molina, M. J., Nenes, A., Penner, J. E., Prather, K. A., Ramanathan, V., Ramaswamy, V., Rasch, P. J., Ravishankara, A. R., Rosenfeld, D., Stephens, G., and Wood, R.: Improving our fundamental understanding of the role of aerosol-cloud interactions in

- the climate system, *P. Natl. Acad. Sci. USA*, 113, 5781–5790, <https://doi.org/10.1073/pnas.1514043113>, 2016.
- Sellar, A. A., Jones, C. G., Mulcahy, J. P., Tang, Y., Yool, A., Wiltshire, A., O'Connor, F. M., Stringer, M., Hill, R., Palmieri, J., Woodward, S., de Mora, L., Kuhlbrodt, T., Rumbold, S. T., Kelley, D. I., Ellis, R., Johnson, C. E., Walton, J., Abraham, N. L., Andrews, M. B., Andrews, T., Archibald, A. T., Berthou, S., Burke, E., Blockley, E., Carslaw, K., Dalvi, M., Edwards, J., Folberth, G. A., Gedney, N., Griffiths, P. T., Harper, A. B., Hendry, M. A., Hewitt, A. J., Johnson, B., Jones, A., Jones, C. D., Keeble, J., Liddicoat, S., Morgenstern, O., Parker, R. J., Predoi, V., Robertson, E., Siahayan, A., Smith, R. S., Swaminathan, R., Woodhouse, M. T., Zeng, G., and Zerroukat, M.: UKESM1: Description and Evaluation of the U. K. Earth System Model, *J. Adv. Model. Earth Sy.*, 11, 4513–4558, <https://doi.org/10.1029/2019MS001739>, 2019.
- Spracklen, D. V. and Rap, A.: Natural aerosol–climate feedbacks suppressed by anthropogenic aerosol, *Geophys. Res. Lett.*, 40, 5316–5319, <https://doi.org/10.1002/2013GL057966>, 2013.
- Steensen, B. M., Schulz, M., Theys, N., and Fagerli, H.: A model study of the pollution effects of the first 3 months of the Holuhraun volcanic fissure: comparison with observations and air pollution effects, *Atmos. Chem. Phys.*, 16, 9745–9760, <https://doi.org/10.5194/acp-16-9745-2016>, 2016.
- Stein, A. F., Draxler, R. R., Rolph, G. D., Stunder, B. J. B., Cohen, M. D., and Ngan, F.: NOAA's HYSPLIT Atmospheric Transport and Dispersion Modeling System, *B. Am. Meteorol. Soc.*, 96, 2059–2077, <https://doi.org/10.1175/BAMS-D-14-00110.1>, 2015.
- Stevens, B. and Feingold, G.: Untangling aerosol effects on clouds and precipitation in a buffered system, *Nature*, 461, 607–613, <https://doi.org/10.1038/nature08281>, 2009.
- Toll, V., Christensen, M., Gassó, S., and Bellouin, N.: Volcano and Ship Tracks Indicate Excessive Aerosol-Induced Cloud Water Increases in a Climate Model, *Geophys. Res. Lett.*, 44, 12492–12500, <https://doi.org/10.1002/2017GL075280>, 2017.
- Toll, V., Christensen, M., Quaas, J., and Bellouin, N.: Weak average liquid–cloud–water response to anthropogenic aerosols, *Nature*, 572, 51–55, <https://doi.org/10.1038/s41586-019-1423-9>, 2019.
- Trofimov, H., Bellouin, N., and Toll, V.: Large-scale industrial cloud perturbations confirm bidirectional cloud water responses to anthropogenic aerosols, *J. Geophys. Res.-Atmos.*, 125, e2020JD032575, <https://doi.org/10.1029/2020JD032575>, 2020.
- Turnock, S. T., Mann, G. W., Woodhouse, M. T., Dalvi, M., O'Connor, F. M., Carslaw, K. S., and Spracklen, D. V.: The Impact of Changes in Cloud Water pH on Aerosol Radiative Forcing, *Geophys. Res. Lett.*, 46, 4039–4048, <https://doi.org/10.1029/2019GL082067>, 2019.
- Twigg, M. M., Ilyinskaya, E., Beccaceci, S., Green, D. C., Jones, M. R., Langford, B., Leeson, S. R., Lingard, J. J. N., Pereira, G. M., Carter, H., Poskitt, J., Richter, A., Ritchie, S., Simmons, I., Smith, R. I., Tang, Y. S., Van Dijk, N., Vincent, K., Nemitz, E., Veno, M., and Braban, C. F.: Impacts of the 2014–2015 Holuhraun eruption on the UK atmosphere, *Atmos. Chem. Phys.*, 16, 11415–11431, <https://doi.org/10.5194/acp-16-11415-2016>, 2016.
- Twomey, S.: Pollution and the planetary albedo, *Atmos. Environ.*, 8, 1251–1256, [https://doi.org/10.1016/0004-6981\(74\)90004-3](https://doi.org/10.1016/0004-6981(74)90004-3), 1974.
- Walters, D., Baran, A. J., Boutle, I., Brooks, M., Earnshaw, P., Edwards, J., Furtado, K., Hill, P., Lock, A., Manners, J., Morcrette, C., Mulcahy, J., Sanchez, C., Smith, C., Stratton, R., Tennant, W., Tomassini, L., Van Weverberg, K., Vosper, S., Willett, M., Browse, J., Bushell, A., Carslaw, K., Dalvi, M., Essery, R., Gedney, N., Hardiman, S., Johnson, B., Johnson, C., Jones, A., Jones, C., Mann, G., Milton, S., Rumbold, H., Sellar, A., Ujjié, M., Whittall, M., Williams, K., and Zerroukat, M.: The Met Office Unified Model Global Atmosphere 7.0/7.1 and JULES Global Land 7.0 configurations, *Geosci. Model Dev.*, 12, 1909–1963, <https://doi.org/10.5194/gmd-12-1909-2019>, 2019.
- Watson-Parris, D. and Smith, C. J.: Large uncertainty in future warming due to aerosol forcing, *Nat. Clim. Change*, 12, 1111–1113, <https://doi.org/10.1038/s41558-022-01516-0>, 2022.
- Wells, A. F., Jones, A., Osborne, M., Damany-Pearce, L., Partridge, D. G., and Haywood, J. M.: Including ash in UKESM1 model simulations of the Raikoke volcanic eruption reveals improved agreement with observations, *Atmos. Chem. Phys.*, 23, 3985–4007, <https://doi.org/10.5194/acp-23-3985-2023>, 2023.
- West, R. E. L., Stier, P., Jones, A., Johnson, C. E., Mann, G. W., Bellouin, N., Partridge, D. G., and Kipling, Z.: The importance of vertical velocity variability for estimates of the indirect aerosol effects, *Atmos. Chem. Phys.*, 14, 6369–6393, <https://doi.org/10.5194/acp-14-6369-2014>, 2014.
- Williams, K. D., Copsey, D., Blockley, E. W., Bodas-Salcedo, A., Calvert, D., Comer, R., Davis, P., Graham, T., Hewitt, H. T., Hill, R., Hyder, P., Ineson, S., Johns, T. C., Keen, A. B., Lee, R. W., Megann, A., Milton, S. F., Rae, J. G. L., Roberts, M. J., Scaife, A. A., Schiemann, R., Storkey, D., Thorpe, L., Watterson, I. G., Walters, D. N., West, A., Wood, R. A., Woollings, T., and Xavier, P. K.: The Met Office Global Coupled Model 3.0 and 3.1 (GC3.0 and GC3.1) Configurations, *J. Adv. Model. Earth Sy.*, 10, 357–380, <https://doi.org/10.1002/2017MS001115>, 2018.
- Wilson, D. R. and Ballard, S. P.: A microphysically based precipitation scheme for the UK Meteorological Office Unified Model, *Q. J. Roy. Meteor. Soc.*, 125, 1607–1636, <https://doi.org/10.1256/smsqj.55706>, 1999.
- Wilson, D. R., Bushell, A. C., Kerr-Munslow, A. M., Price, J. D., Morcrette, C. J., and Bodas-Salcedo, A.: PC2: A prognostic cloud fraction and condensation scheme, II: Climate model simulations, *Q. J. Roy. Meteor. Soc.*, 134, 2109–2125, <https://doi.org/10.1002/qj.332>, 2008a.
- Wilson, D. R., Bushell, A. C., Kerr-Munslow, A. M., Price, J. D., and Morcrette, C. J.: PC2: A prognostic cloud fraction and condensation scheme, I: Scheme description, *Q. J. Roy. Meteor. Soc.*, 134, 2093–2107, <https://doi.org/10.1002/qj.333>, 2008b.
- Wood, R.: Stratocumulus Clouds, *Mon. Weather Rev.*, 140, 2373–2423, <https://doi.org/10.1175/MWR-D-11-00121.1>, 2012.
- Wood, R. and Bretherton, C. S.: On the Relationship between Stratiform Low Cloud Cover and Lower-Tropospheric Stability, *J. Climate*, 19, 6425–6432, <https://doi.org/10.1175/JCLI3988.1>, 2006.
- Woodward, S.: Modeling the atmospheric life cycle and radiative impact of mineral dust in the Hadley Centre climate model, *J. Geophys. Res.-Atmos.*, 106, 18155–18166, <https://doi.org/10.1029/2000JD900795>, 2001.
- Zerefos, C. S., Eleftheratos, K., Kapsomenakis, J., Solomos, S., Inness, A., Balis, D., Redondas, A., Eskes, H., Allaart, M., Amiridis, V., Dahlback, A., De Bock, V., Diémoz, H., Engelmann, R., Eriksen, P., Fioletov, V., Gröbner, J., Heikkilä, A.,

Petropavlovskikh, I., Jaroslowski, J., Josefsson, W., Karppinen, T., Köhler, U., Meleti, C., Repapis, C., Rimmer, J., Savinykh, V., Shirov, V., Siani, A. M., Smedley, A. R. D., Stanek, M., and Stübi, R.: Detecting volcanic sulfur dioxide plumes in the Northern Hemisphere using the Brewer spectrophotometers, other networks, and satellite observations, *Atmos. Chem. Phys.*, 17, 551–574, <https://doi.org/10.5194/acp-17-551-2017>, 2017.

Zhang, S., Wang, M., Ghan, S. J., Ding, A., Wang, H., Zhang, K., Neubauer, D., Lohmann, U., Ferrachat, S., Takeamura, T., Gettelman, A., Morrison, H., Lee, Y., Shindell, D. T., Partridge, D. G., Stier, P., Kipling, Z., and Fu, C.: On the characteristics of aerosol indirect effect based on dynamic regimes in global climate models, *Atmos. Chem. Phys.*, 16, 2765–2783, <https://doi.org/10.5194/acp-16-2765-2016>, 2016.